Master thesis

The nature of the Pamir subduction zone derived from stress field modelling

B. L. Vogelaar

Utrecht University, Faculty of Geosciences

Supervisor: dr. R. Govers

Utrecht University, Faculty of Geosciences

Universiteit Utrecht

October 25, 2013

Abstract

In this thesis a new approach is tested to determine the nature of the subduction processes occurring in the Pamir orogen. The occurrence of subduction underneath the central Pamir Mountains, located on the eastern border of Afghanistan and Tajikistan, has been subject to discussion for more than three decades. Seismic imaging and earthquake data of the area have shown a slab up to a few hundred kilometres deep, but whether it is continental or oceanic material subducting has not yet been conclusively decided. In this thesis we construct a model of the stress field of the region as a consequence of long wavelength forces and the slab pull in the Pamir region. We test several slab pull scenarios corresponding to continental or oceanic subduction. The resulting stress fields are compared to stress observations to find whether including the subduction processes gives a better fit. We compare the instantaneous displacements associated with the applied tractions to the movement of the region as obtained through GPS. A range of scenarios is tested to account for geometry and material properties. Our preferred model is the model with a neutrally buoyant slab of Eurasian origin. This implies that active continental subduction is taking place in the Pamir mountains.

1 Introduction

The Pamir-Hindu Kush orogen (location, see fig 1a) is a consequence of the collision of the Eurasian and Indian plates, which is estimated to have initiated in this region around 55 Ma (Klootwijk et al., 1992; Guillot et al., 2003). Since 25 Ma the Pamir region has moved north by about 300 km relative to surrounding areas (Sobel and Dumitru, 1997) overriding most of the Tajik-Yarkand Basin (Burtman and Molnar, 1993). Another 300 km of shortening has been accommodated through internal deformation (Burtman and Molnar, 1993). This deformation seems to be ongoing: a velocity discontinuity derived from GPS data indicates that thrusting is still occurring (see fig 1b) across the Main Pamir thrust, which is thought to be the surface expression of a slab underneath the Pamir (see figures 1a and 1d). This fault is located well north of the boundary of Eurasian and Indian plates as defined by Bird (2003) and so this would indicate intracontinental subduction. Two scenarios concerning this relatively uncommon process are currently prevailing. The first scenario favours the subduction of the Eurasian continent in the Pamir and subduction of Indian ocean beneath the Hindu Kush. In this scenario there are two opposing subducting plates in close proximity (Burtman and Molnar (1993); Fan et al. (1994); Negredo et al. (2007)). In the second scenario, Indian oceanic lithosphere is subducting along the whole length of the fault, but underneath the Pamir orogen the slab has been detached and overturned (Pegler and Das (1998); Koulakov and Sobolev (2006)). Recently a third scenario was proposed by Sippl et al. (2013b), based on a geometry derived from new earthquake data. They propose that the slab in the entire Pamir-Hindu Kush region is part of the Eurasian continent, but has overturned and is possibly detached underneath the Hindu Kush mountains. Geological observations (Burtman and Molnar (1993)) indicate northward overthrusting of the Pamir and hence the second scenario seems unlikely. This is reinforced by more recent studies which, through higher resolution imaging, show that the origin of the slab is most likely Eurasian (Mechie et al., 2012; Sippl et al., 2013b). However, there is no strong evidence yet which favours the first or the third scenario. Together with the origin, the nature of the subducted material also remains debated with suggestions for oceanic subduction (Chatelain et al., 1980), continental subduction (Hamburger et al., 1992; Burtman and Molnar, 1993) or a mix of both (Mellors et al., 1995).

In this study we use a new approach to constrain the nature and origin of the subducting material in the Pamir region by modelling the effect of the occurrence of subduction on the stress field in the region. We use a model of the stress field of the Eurasian plate using a combined lithosphere-mantle approach similar to a model by Warners-Ruckstuhl et al. (2013). The forces acting on the Eurasian plate (divided in lithospheric body forces, edge forces and mantle tractions) are estimated and constrained using the principle of torque balance (Forsyth and Uyeda, 1975) to generate a dynamically consistent intraplate stress field of Eurasia. In the model by Warners-Ruckstuhl et al. (2013) the Main Pamir thrust is not included, which is equivalent to a 'locked' subduction contact, i.e. there is no differential displacement.

In this study a thrust fault representing the Main Pamir Thrust and forcing corresponding to a slab will be included. A range of scenarios, including the aforementioned ones, are tested. The modelled stress fields are then compared quantitatively to the observations gathered in the World Stress Map project (Heidbach et al., 2008) and the displacements of the region are compared to recent studies on GPS in the region (Reilinger et al., 2006; Mohadjer et al., 2010; Zubovich et al., 2010). From the fit of the models to observations we can then constrain the most likely scenario and so determine nature of the subducted material.

2 Tectonic setting

2.1 Geometry and mantle structure

The Pamir and Hindu-Kush orogens are located on the diffuse (Bird, 2003) boundary of the Indian and Eurasian plate. The Pamir-Hindu Kush region is heavily faulted with the Main Pamir Thrust being of particular importance for this study (see figure 1a).

From seismic tomography and relocated earthquake hypocenters (for example Pegler and Das (1998); Koulakov and Sobolev (2006); Negredo et al. (2007); Zhang et al. (2011); Sippl et al. (2013b)) the outline of a slab can be traced through most of Pamir-Hindu Kush region, forming an approximately S-shaped curve (see figure 1c). In the central Pamir this slab dips southwards at about 45°and can be found to a depth of approximately 350 km (with earthquakes occurring to a depth of approximately 200km, see figure 1d). In the western Pamir the slab dips south-eastwards at a steeper angle, varying between 70 and almost 90°. The slab also reaches greater depths in this region, up to about 450 km depth (Negredo et al., 2007; Sippl et al., 2013b). More to the west, underneath the Hindu Kush orogen, a north-dipping slab can be traced (Pegler and Das, 1998; Negredo et al., 2007; Sippl et al., 2013b). This slab subducts at an angle of almost 90° and reaches depths up to 500 km. A tear between the Pamir and Hindu Kush slabs is generally imaged in slab geometries of this region (Mattauer, 1986; Negredo et al., 2007; Sippl et al., 2013b). This leads to a geometry with two separated slabs subducting at steep angles in opposite directions (see figure 2a).

The thickness of the crustal part of the slab can be estimated from seismicity data since the majority of the earthquakes will be located in the (rheologically different) crustal part of the slab. Earthquake relocation studies by Pegler and Das (1998) and Sippl et al. (2013b) both find that the majority of the epicentres are located in a band of 10-20 km thickness on a total slab thickness of 100 km. This is fairly consistent with structural studies of the region, which estimate that the pristine lithosphere consists of about 40 km crust and 80 km lithospheric mantle (Beloussov and Belyaevsky, 1980), but for subducted lithosphere the upper crust is scraped off (Burtman and Molnar, 1993) and the lower crust is thinned through extension (after Leith and Alvarez (1985)), allowing for crust of 20-25 km thickness to be subducted. For the Pamir subduction zone this leads to a geometry of a curved subduction zone with a south-dipping slab of Eurasian origin, where only the lower crust is incorporated to mantle depths (see fig 2b).

2.2 Slab composition

Due to the similarity of the Wadati-Benioff zones found in the Pamir and in oceanic subduction settings, it was originally thought that the subducted slab was of oceanic origin (Chatelain et al., 1980). Slab imaging through tomography could not confirm this hypothesis, with studies finding both anomalously high velocities (indicating crustal material, Roecker, 1982) and low velocities (indicating oceanic material, Mellors et al., 1995). The presence of oceanic material is now thought unlikely because indirect geological observations prefer material of continental origin. So is The Pamir-Hindu Kush zone located well north of the Indus-Yardung suture, where the last remnants of the Tethys ocean were subducted (Sippl et al., 2013b), there is no evidence of oceanic material in the stratigraphy north of the Indus-Yardung Suture (Burtman and Molnar, 1993) and there is also a distinct lack of oceanic island arc volcanics in the region (Hamburger et al., 1992).

Reconstructions of the region from structural geology (Hamburger et al., 1992; Lukk et al., 1995) and the presence of xenoliths of crustal origin in parts of the Pamir orogen (Budanova, 1991; Searle et al., 2001; Ducea et al., 2003; Gordon et al., 2012) both indicate that crustal material has been displaced to great depths (at least 70 km), so a supply of crustal material which could possibly

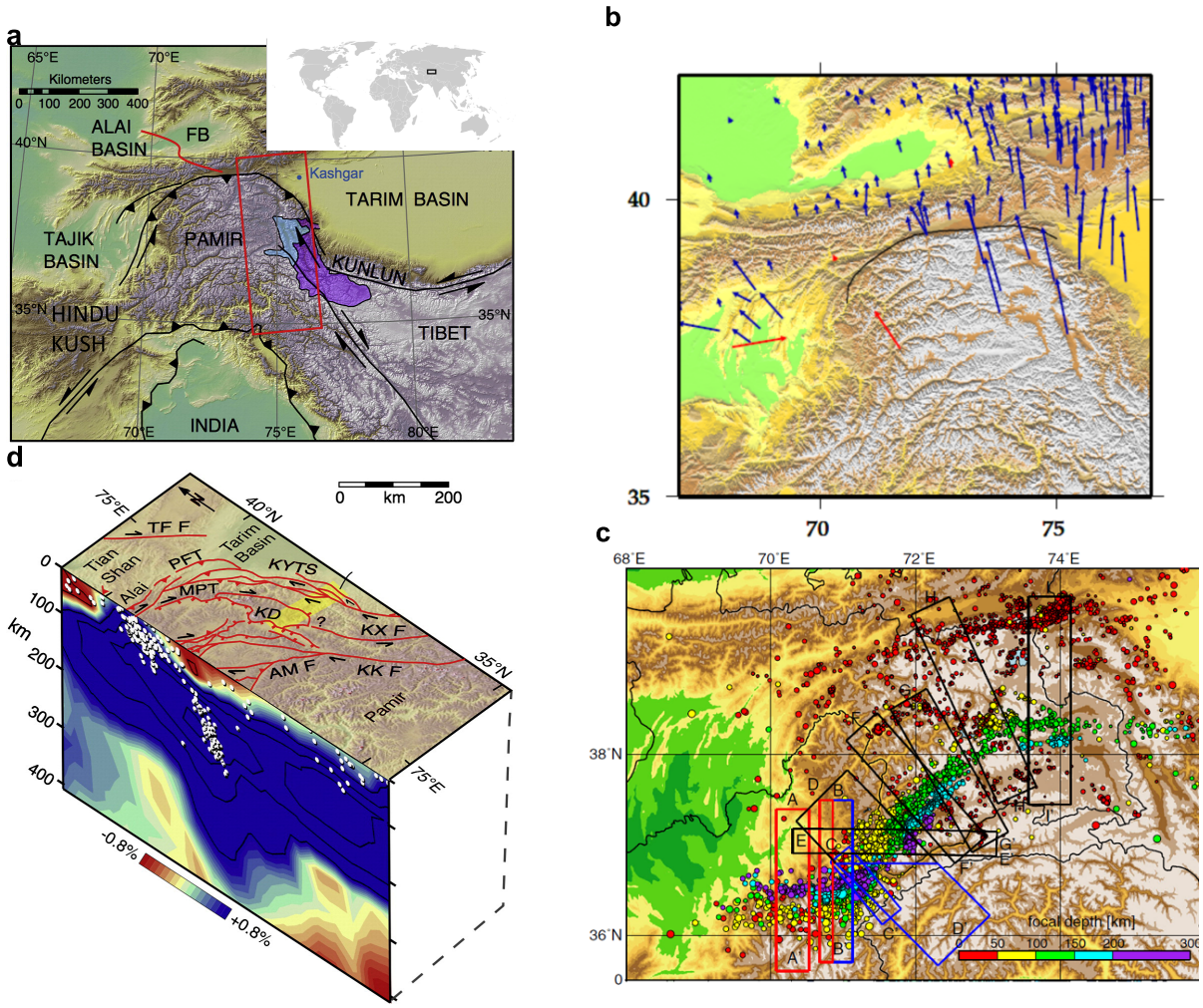

Figure 1: Description of figures, clockwise, starting at top left. a) Location of the Pamir mountains and large scale tectonic structures therein. The Hindu Kush is located to the south west of the Pamir mountains. The subduction zone studied in this thesis surfaces at the Main Pamir Thrust (MPT), which is the upper thrust fault in this figure. Red box indicates the location of d. Black box in the inset shows the location of this image on a world map. b) Displacements relative to a fixed Eurasian plate for the Pamir region. A sharp decrease in velocity can be observed across the Main Pamir Thrust (black line). No trend in velocity can be discerned within the Pamir region south of this fault. c) The location of the slab as traced through seismics. Earthquakes at depth greater than 50 km line up to create a flattened S-shape. d) Cross-section through the Eastern Pamir, showing local structures and tomography. White dots indicate (relocated) earthquake epicentres. Both tomography and earthquake distribution indicate a slab present. Figures a) and d) modified from Sobel et al. (2011), with tomography based on Negredo et al. (2007), figure b) contains data from Zubovich et al. (2010) (black arrows) and Mohadjer et al. (2010) (red arrows), figure c) after Sippl et al. (2013b).
Abbreviations figures a): FB: Ferghana Basin; and d): TFF: Talas Ferghana Fault, KYTS: Kashgar Yecheng Transfer System, MPT: Main Pamir Thrust, PFT: Pamir Frontal Thrust, KXF: Karakax Fault, KKF; Karakoram Fault, AMF: Aksu Murgab Fault, KD: Kongur Detachment.

(a) Simplified Pamir-Hindu Kush geometry

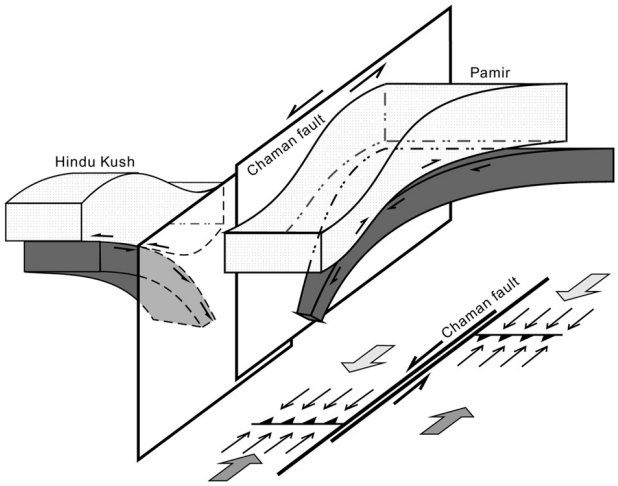

(b) Detailed Pamir geometry

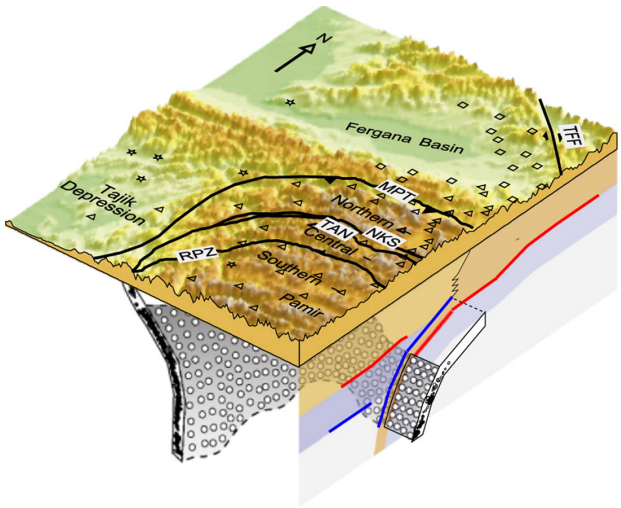

Figure 2: a) A simplified geometry of the Pamir-Hindu Kush zone, showing the north dipping Hindu Kush slab and south dipping Pamir slab, separated by a large vertical tear. Image after Zhang et al. (2011). b) A more detailed geometry of the Pamir subduction zone derived from our interpretation of available literature: a curved, south-dipping European slab with only the lower crust (indicated by the thin brown band in the subduction zone) actively subducting together with the lithospheric mantle. Vertical scaling is exaggerated for topography and crustal thickness (brown colours) compared to lithospheric thickness (grey colour). Image after Schneider et al. (2013). Abbreviations: MPT: Main Pamir Thrust, TFF: Talas Ferghana Fault, NKS: North Pamir/Kunlun Suture, TAN: Tanymas Suture, RPZ: Rushan Pszart Zone.

subduct is present. However, neither study has actual proof of material being displaced to depths over 100 kilometres, which would be a stronger indication for actual subduction.

No constraint can be placed on the geochemistry of this deep crustal material from geological evidence, since both felsic (light) and mafic (dense) lower crustal rocks are found in the remnants of the Alai Basin (Leith and Alvarez, 1985). As for the lithospheric mantle, there is no indication for an anomalous mantle structure and for current depth levels of the slab (350 km) the olivine-spinel transition (at 410 km, (Sung and Burns, 1976)) has not been passed.

2.3 Observations on regional stress and displacement fields

Observations on the world stress field are collected by the World Stress Map (WSM) project (Heidbach et al., 2008). Data from the WSM database is compared with the modelled stresses and so the modelled stress field can be tested. The used WSM data contains the azimuth of the maximal horizontal stress from observations up to 100 km depth. The data quality in the region of interest is relatively poor with only 1% of the with an uncertainty of less than $\pm 20°$. All other observations have an uncertainty of $\pm 25°$, which will be taken as the uncertainty for the rest of this study. The stress directions and the quality of the corresponding measurements used for this study can be found in figure 3.

Observations on the local displacement field have been gathered in several GPS studies. All displacements are presented in a fixed Eurasian reference frame and so are relative displacements. These displacements can be found in figure 4.

3 Model set-up

The nature of the subduction zone in the Pamir region is determined through a stress field model of the region. Stresses in the model are a consequence of both long wavelength forcing (for example

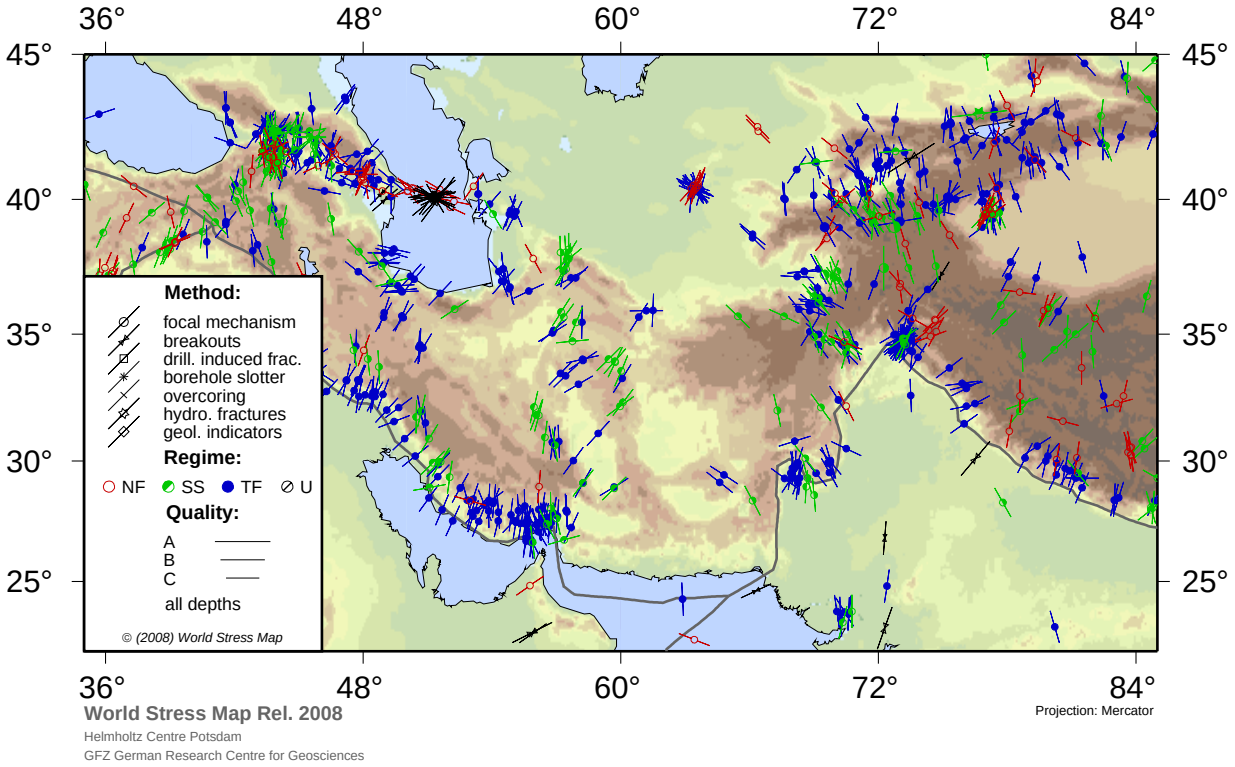

Figure 3: Stress data used in this study, as gathered from the WSM project Heidbach et al. (2008). Abbrevations: NF: normal, SS: strike slip, TF: thrust fault, U: undetermined. Quality refers to uncertainty of $\pm$ 15˚ (A), $\pm$ 20˚ (B) and $\pm$ 25˚ (C).

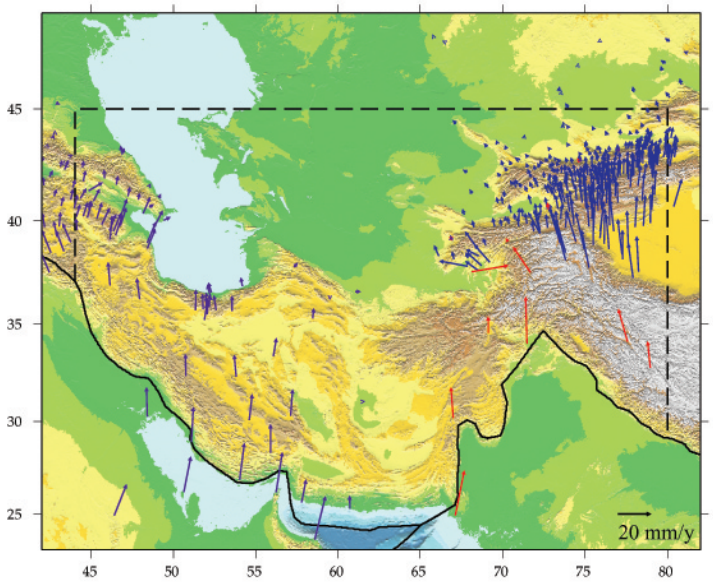

Figure 4: GPS velocities in the region of interest. Data is obtained from Zubovich et al. (2010)(blue arrows), Mohadjer et al. (2010)(red arrows) and Reilinger et al. (2006)(purple arrows). The last dataset included data from earlier studies, mainly by Vernant et al. (2004). The continuous black line is part of the plate boundary of the Eurasian plate as defined by Bird (2003). The dashed black line indicates the 'inner boundary' of the modelled region (see text and figure 5).

plate-plate interaction and the tractions exerted by the viscous mantle) and the forcing of the slab underneath the Pamir. In this section we will explain in some detail our choices for the modelling approach, the model geometry and the boundary conditions.

3.1 Stress modelling

In this thesis, the focus is on calculating elastic stresses, since the first response of lithosperic material to forces is to deform elastically. More advanced calculations (including plasticity, strain rates and/or rotation rates) require detailed knowledge of the rheological properties, which is beyond the scope of this thesis. To calculate these stresses we create a 2D model of the region assuming plane stress and using spherical elements. The finite element code GTECTON (Govers and Meijer, 2001) is used to solve the mechanical equilibrium equations required to obtain the stresses. The values of the elastic properties of the lithosphere in this study are 70 GPa for Young's modulus and a value 0.25 for Poisson's ratio. The fault is assumed to be frictionless and is modelled using slippery nodes (Melosh and Williams, 1989). As in the study by Warners-Ruckstuhl et al. (2013) (hereafter: WR) the focus will only be on the stress direction and not on magnitude. Stress directions are assumed not to be affected by viscous relaxation or displacement on randomly oriented minor faults, whereas stress magnitudes presumably are affected by these features.

The mesh for this FE program is created using the software Triangle (Shewchuk, 1996). Preset nodal points are used to define the main features of the model: the boundaries and the location of the Pamir subduction zone. Additional nodal points are to create a high quality grid with a maximum element area of 0.3 square degrees. The thickness of the elements is 100 km, corresponding to the lithospheric thickness in the region (Conrad and Lithgow-Bertelloni, 2006). With the assumption that the stress field is not affected by variations in lithospheric thickness the stress field integrated over the lithostatic column is then calculated. Convergence tests were not conducted because the grid used in this study has mostly the same features and a higher grid density than the grid used by WR, where convergence was achieved. The main difference between the two studies, the active fault, would ideally require a convergence test, but due to time constraints no convergence was achieved.

3.2 Model geometry and plate boundaries

The model boundaries are set at the boundary of the Eurasian and Anatolian plates (as defined by Bird (2003)), a north-south line at 85° E, a north-south line at 36° E and an east-west line at 65° N, where the Eurasian and Anatolian plate are assumed one coherent unit. With these boundaries, the region of interest, bound to the south by the boundary of the Eurasian plate and a north-south line at 80° E, a north-south line at 44° E and an east-west line at 45° N, will not be influenced by edge effects. Another consequence of the choice for these boundaries is that the influence of unwanted regional tectonic features (faulting associated with the Anatolian plate, the geologically complex Himalayas) is reduced to a minimum. The model boundaries and the boundaries of the region of interest can be found in figure 5.

3.3 Boundary conditions

Boundary conditions in this model include the mantle tractions, edge forces on both inner and outer edges, body forces and anchor points. All boundary conditions except for the anchor points represent the conditions outside the model domain assumed to influence the lithospheric stress field. The anchor points (zero displacement nodes) are required for successful computation of the results and as well as a comparison of the velocities, which requires a fixed Eurasian frame. The anchor points have

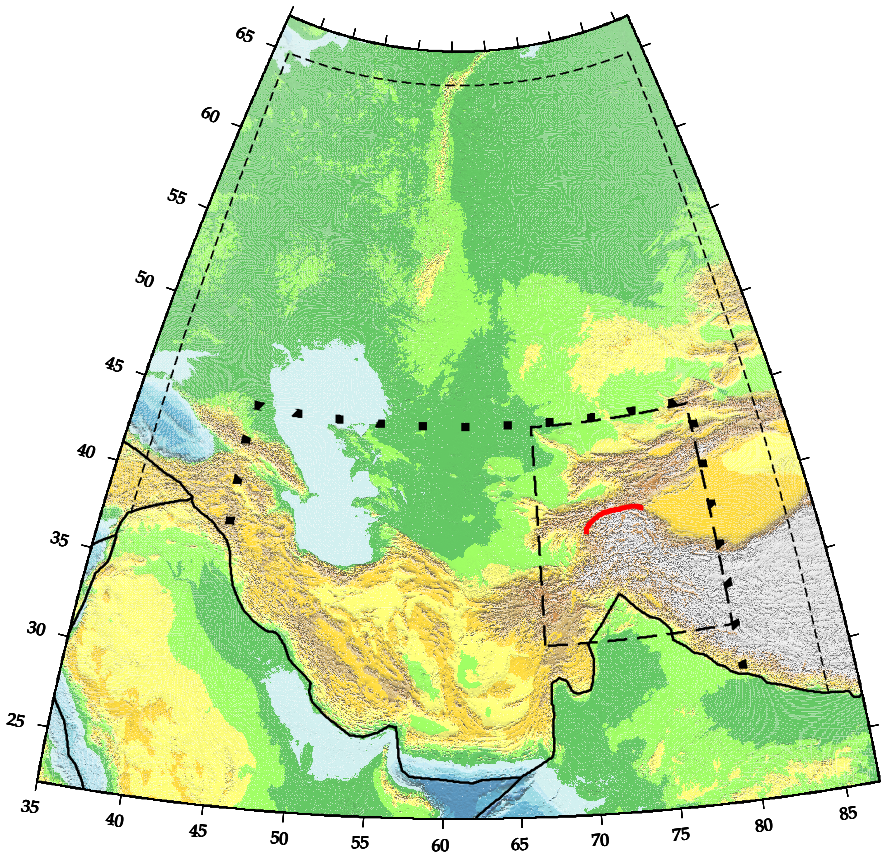

Figure 5: The model domains and subdomains used in this study. The model domain is bound by the predefined boundaries (thin dashed lines) and the Eurasian plate boundary as defined by Bird (2003) (black line). The region of interest or 'Inner region' is bound by the dotted black line and the plate boundary and will be used to display the results. The 'Pamir subdomain' is used for comparing results locally and is bound by the thick dashed line. The location of the Main Pamir thrust, where subduction is expected to occur, is indicated by the red line.

been placed at locations where their influence on the results should be minimal. The approach to obtain the boundary conditions follows methods used by WR and will only be summarized here. Where WR tested for a range of models for mantle flow and lithospheric body forces (LBF's), here only one mantle flow model (nGrand Grand, 2002) and one LBF model (*Lithodens*) are used. These are chosen since the preferred model of WR (EUR2best) is produced using these models and our results are benchmarked with this model. For the conversion from tractions obtained in the following sections to nodal points forces (which the models require as input for boundary conditions) and a more extensive overview of the methods used as well as a sensitivity analysis on the location of the anchor points, you are referred to appendix A.

3.3.1 Mantle tractions

Mantle tractions arise from the flow of highly viscous mantle material underneath the more rigid lithosphere. In this study, mantle tractions are calculated based on the nGrand mantle flow model (Grand, 2002) using the user interface SEATREE (Milner et al., 2009). The radial viscosity profile used for these calculations comes from Simmons et al. (2009), modified after Mitrovica and Forte (2004). Two effects on the lithosphere are accounted for: direct forcing by shear stresses at the bottom of the plates and indirect forcing by normal stresses inducing dynamic topography, which in turn affect LBF's. The mantle tractions used as input by WR in model EUR2best could not be reproduced by this study: the normal stresses are reproduced with some degree of accuracy but there is a significant difference in the direction and magnitude of the shear tractions.

3.3.2 Lithospheric body forces

For calculations of the lithospheric body forces we assume lithostatic pressure, generally calculated as a vertical pressure, to be isotropic and the lithosphere to be in isostatic equilibrium. Variations in topography and density structure of the lithosphere are the cause of pressure gradients. These pressure gradients give rise to horizontal forces acting on the lithosphere which in turn affect the stress field of the lithosphere (Artyushkov, 1973; Molnar and Lyon-Caen, 1988); These will be referred to as the lithospheric body forces (LBF's).

In continental domains the variations in density and topography are hard to constrain. Since the modelled domain consists entirely of continental lithosphere (assuming the continental shelf on the southern margin of the domain to have a continental lithosphere), this brings a measure of uncertainty to the results. Therefore, the model *Lithodens* from WR is used to calculate the LBF's in the model. *Lithodens* combines crustal structure from Crust2.0 (Bassin et al., 2000), topography from the ETOPO1 dataset (Amante and Eakins, 2009) and normal stresses from mantle flow modelling as described in the previous section. Remaining topography variations are assumed to be caused by density variations in the lithospheric mantle.

3.3.3 External forces

This model uses three types of edge forces. Along the southern boundary of the model the forces that arise due to mechanical interaction with neighbouring plates are applied. The southern boundary has been divided into three segments along which the forcing varies representing both normal collision of the Indian and Arabian plates with Eurasia as well as the highly oblique collision of the Indian plate along its western edge. The forcing is modelled anti-parallel to the relative motion of the adjacent plate (taken from Nuvel-1A, DeMets et al. (1994)) along the entire southern boundary and is assumed uniform (with values of 2.0 TN/m, 1.0 TN/m and 9.8 TN/m, respectively) along a segment. Along

the predefined boundaries the tractions that are the consequence of the stress field as modelled by WR are applied.

3.3.4 Pamir subduction

The model has one internal edge, which represents the Pamir subduction zone. The pull on this zone is dependent on slab geometry and material parameters (McKenzie, 1969). From section 2.1 we can constrain the geometry of the slab with reasonable certainty but the nature of the subducted material is less certain, as discussed in section 2.2. For this reason we will test scenarios ranging from very buoyant continental crust to very dense oceanic or eclogitized crust. Although we are reasonably sure about the geometry and hence the direction of forcing, for scientific reasons the direction of the forcing will be varied as well. An overview of all scenarios can be seen in figure 6.

The net slab pull consists of three components: the slab pull as a consequence of dense lithospheric mantle sinking in the asthenosphere (F_{sp}); the viscous resistance of the asthenosphere to this downward motion (F_{vr}); and the compositional buoyancy of the crust (F_{cb}). It is assumed that the directions of the latter two forces are antiparallel to the first. For the models representing subduction of buoyant crust we assume the extreme case of a neutrally buoyant slab and hence zero net slab pull. For the models at the other end of the spectrum, i.e. where crustal material will have turned to highly dense eclogite, we determine the forcing through the steps below. The other models will have a pull somewhere between these two extremes.

The slab pull (F_{sp}) as a consequence of the subduction of dense material can be calculated through the following equation:

$$F_{sp} = gsin(\gamma) \int_0^L \int_0^S (\rho_l - \rho_a) dx dz \tag{1}$$

Symbols, data and sub-equations used are summarized in table 1. The temperature profile on which ρ_l depends is based on GDR1 (Stein and Stein, 1992). Since the values of this model converge for great ages, we have assumed an age of 100 Ma for the slab.

For eclogitized crust the density contrast between mantle material and eclogite is assumed small and the buoyancy force may be negligible or even negative (Cloos, 1993). As a lower bound we will assume a value of 0 TN/m for F_{cb}. Of the viscous resistance relatively little is known and so we will assume a lower bound of 0 TN/m for F_{vr} as well. Both these assumptions will be reviewed in the discussion.

Equation (1) gives an estimate of 16 TN/m for the upper bound of the slab pull along the Pamir subduction zone. Since the lower bounds for both resisting forces are 0 TN/m this gives an upper limit for the net slab pull of 16 TN/m.

3.4 Comparison

For benchmarking purposes, we first construct a model where the subduction contact is 'locked' (the fourth scenario in figure 6). The results of this model should match the results from the model EUR2best from Warners-Ruckstuhl et al. (2013). When this model has been successfully reproduced, forcing corresponding to the features in the Pamir subduction zone (the other scenarios in figure 6) will be added and differential displacement on the fault will be allowed.

Two aspects of the model results (maximum horizontal stress direction and displacement direction) will be compared to observations of these quantities. The modelled stress field will be compared to the observed stress field data as collected by the WSM (Heidbach et al., 2008) (fig. 3). Since the location and sampling of the observed stress data is highly irregular, an averaging grid is developed

Table 1: Values used in slab pull calculation

Parameter	Value	Description	Source
S	$\sqrt{2}\cdot 350$ km	Slab length	Negredo et al. (2007)
L	100 km	Lithospheric thickness	Beloussov and Belyaevsky (1980)
γ	45 °	Slab dip	Negredo et al. (2007)
ρ_a	3.30 kg/m^3	Astenospheric density	Cloos (1993)
α	$4 \cdot 10^{-5}$ C^{-1}	Thermal expansion coefficient	McKenzie (1969)
T_a	1200 °C	Reference mantle temperature	-
C_p	1171 J kg^{-1} K^{-1}	Specific heat	Stein and Stein (1992)
k	3.138	Thermal conductivity	Stein and Stein (1992)
v	3 cm/y	Subducting plate velocity	-
g	10 m/s^2	Gravitational acceleration	-
τ	100 MA	Age of the lithosphere	-
z	0 - L	Distance across slab	-

Parameter	Equation	Description	Source
ρ_l	$\rho_a(1-\alpha(T_{slab}-T_a))$	Lithospheric mantle density	McKenzie (1969)
T_{slab}	$T_a\left(\frac{z}{L}+\sum_{n=1}^{N} c_n exp(\frac{-\beta_n v\cdot\tau}{L})sin(\frac{n\pi z}{L})\right)$	Slab temperature profile (GDH1)	modified after Stein and Stein (1992)
β_n	$\sqrt{R^2+n^2\pi^2}-R$	-	Stein and Stein (1992)
c_n	$\frac{2}{n\pi}$	-	Stein and Stein (1992)
R	$\frac{v\cdot L}{2\cdot\kappa}$	Peclet number	Stein and Stein (1992)
κ	$\frac{k}{\rho_a C_p}$	Thermal diffusivity	Stein and Stein (1992)

and the resulting average misfits are compared (see appendix B for the exact procedure). We have chosen a grid size of 0.5 by 0.5° since this gives the lowest average observational uncertainty. This in turn places maximum constraints on our model results.

The second comparison is between modelled and observed plate velocities in the region (see figure 4). The results of this model are the results of an instantaneous stress field and as such there is no time dimension involved. Consequently there is no velocity output. An indirect comparison is made between the directions of displacement of the model and the observed velocities. Since the observations and model data points are not always located at the same location, the observations and data points are averaged using the same averaging method as used for stresses.

4 Results

4.1 The 'locked' model

In figure 7 a comparison of the original stress field and the stress field as produced by the 'locked' model in this paper is shown. In this figure the directions of the maximal horizontal stresses of both models, as well as the misfit between these directions are mapped. Both the magnitude and the direction of the original stress field are quite well reproduced by the new model. The average misfit angle between the two models is 16°, but more than 70 % of the data has an error margin of smaller than 10°. More important, the average misfit in the Pamir subregion is only 12°.

Next the modelled stress field is compared with the observed stress field (figure 8). The results are similar to those obtained by WR: the Zagros region and northern Himalayas/Pamir region match pretty well, whereas the lower Himalayas and the central region show a significant misfit. The region around the Caspian sea gives mixed results in both models.

The average misfit with the observations over the whole region in the new model is 33° and in the Pamir subregion the misfit is 31°. The misfits in the Zagros (31°) and Tibet (26°) subregions of the model by WR, which cover respectively a large and a small part of the region modelled in this thesis show a marked difference. This difference is the consequence of the smaller averaging grid

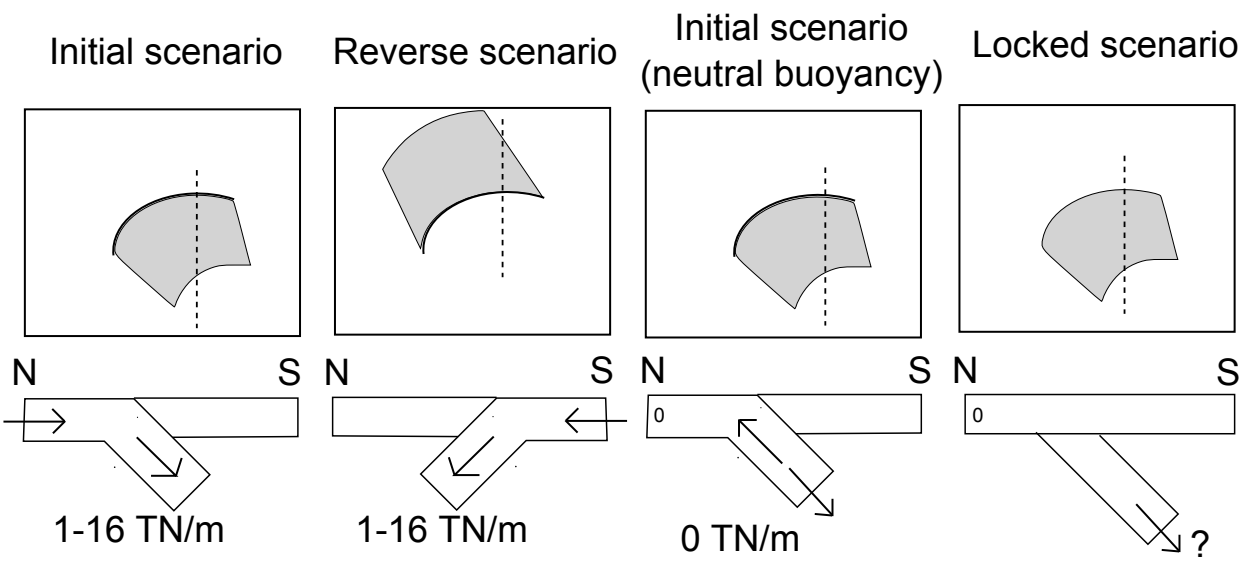

Figure 6: A schematic overview of the models tested in this thesis. The top row contains a map view of the area at approximately the same location as 1a. The location of the fault indicated by the continuous black line and the location of the slab indicated with the grey region. The dashed line indicates the location of the cross sections that can be observed in the lower row. The 'initial scenario' has a south dipping slab, with variable forcing and movement allowed on the fault. The 'reverse scenario' has a north dipping slab, variable forcing and movement allowed on the fault. For the scenarios with neutral buoyancy the slab does not exert a force on the plate and as such the force felt at the surface is zero. Since the slab does not exert a force the dip direction is irrelevant in this scenario. In the 'locked scenario', no movement on the fault is allowed and hence the fault is not explicitly modelled. The presence of the slab does not directly influence the stress field at the surface.

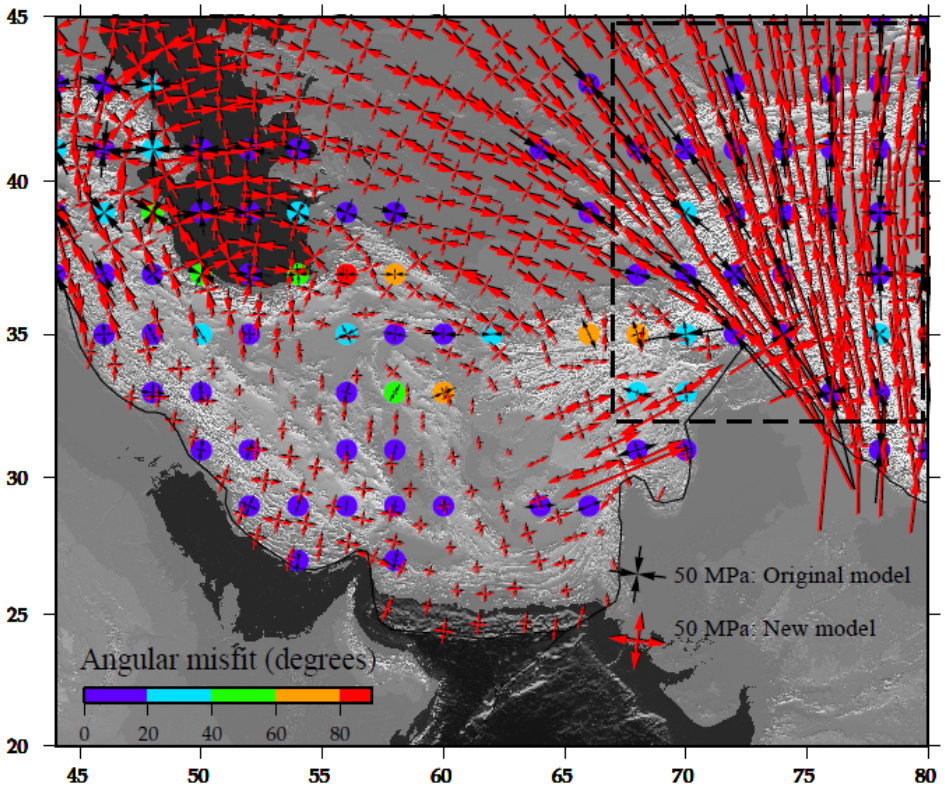

Figure 7: The stress field by WR in black and the stress field as generated in this paper in red. The region shown coincides with the 'Inner region' of figure 5. Data density of the model is higher, but for clarity only a fraction of the stress tensors are shown in this figure as well as figures 8, 9, 11 and 12. The thin black line is part of the plate boundary of the Eurasian plate as defined by Bird (2003). The dashed line indicates the Pamir subregion.

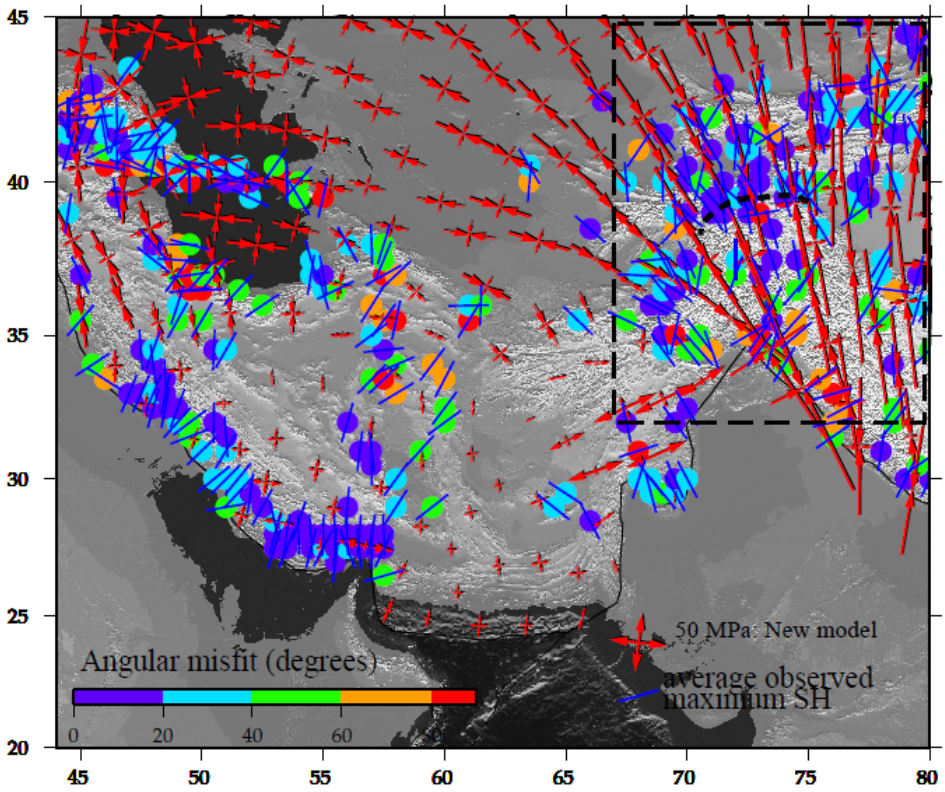

Figure 8: The stress field based on the observations collected by the WSM project compared to the stress field constructed by the locked model in this paper. The location of the Pamir fault is indicated with the thick dashed black line. The thin dashed line indicates the Pamir subregion.

used in this study compared to the grid used by WR. If the data is sampled using a 2x2° grid rather than a 0.5x0.5° grid, the misfits are 30° and 25° for the whole model and the Pamir subregion, respectively, which coincides better with results of WR.

4.2 Pamir subduction

We first present the results of the 'initial scenario' (the first scenario in figure 6). Initially the forcing was set to the maximum value of 16 TN/m. The forcing of the slab is then gradually decreased up to the point where the slab is neutrally buoyant. The average misfit for the whole region and for the Pamir subregion as function of the forcing on the Pamir slab can be found in figure 10a. The results at the lower end of the spectrum have lowest misfit. The best result obtained for this scenario is with a perfect neutrally buoyant slab and will be referred to as *EUdynabest* and the resulting stress field for this model can be found in figure 9. The misfit in the Pamir subregion increases in all subduction models with respect to the locked model. However, the fit in the locked model with the observations for the region north and north-west of the Pamir fault zone is quite good already. The modelled data in the region south-east of the Pamir fault does not have quite as good a fit. So although geological evidence favours Eurasian subduction, we show the results for an Indian plate underthrusting the Eurasian plate as well (referred to as 'reverse scenrio', second scenario in figure 6).

In general, this model produces better results than the initial scenario. The scenario where a force of 8 TN/m is applied gives the best overall results (and this model will be referred to as *INDynabest*). The misfit in the Pamir subregion increases by 0.8° but the misfit over the whole region decreases by 2.2° with respect to the locked model. Figure 11 shows the stressfield of this scenario.

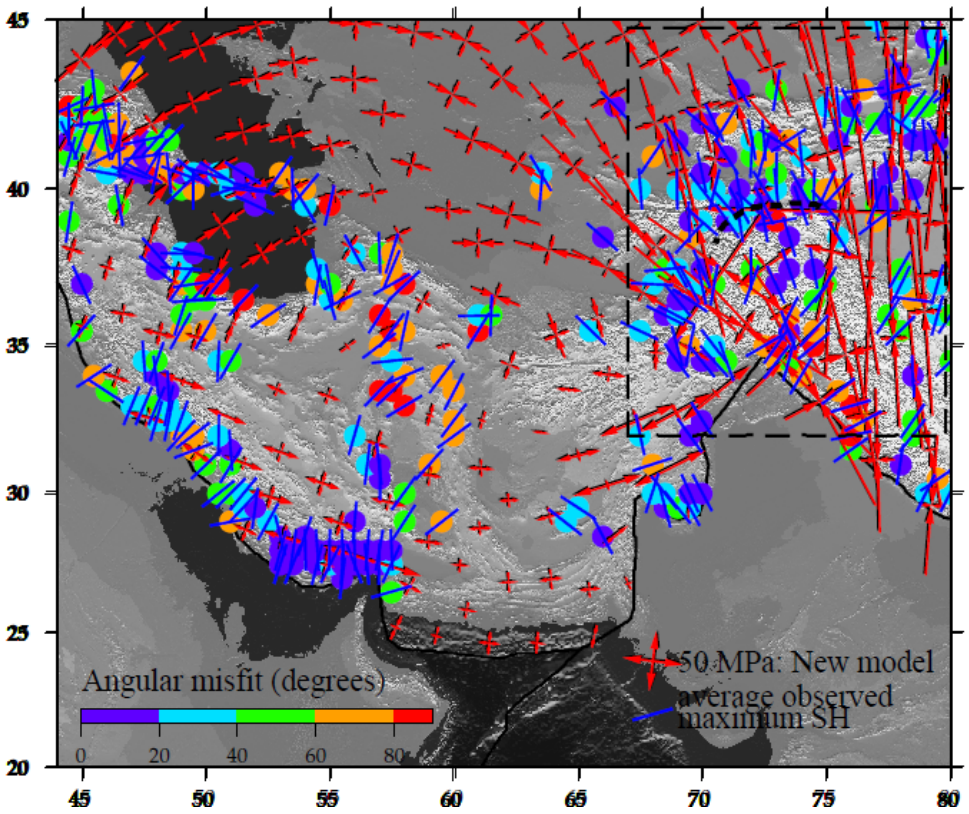

Figure 9: The stress field based on the observations collected by the WSM project compared to the stress field constructed in the scenario where the slab pull on the Pamir is neutrally buoyant (model *EUdynabest*).

(a) Normal scenario

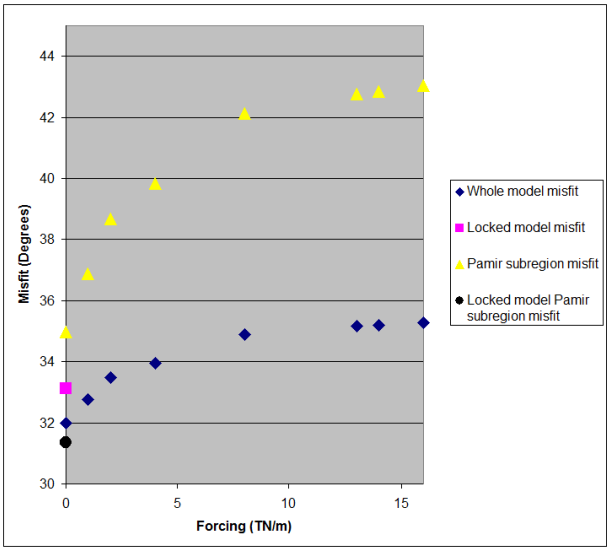

(b) Reverse scenario

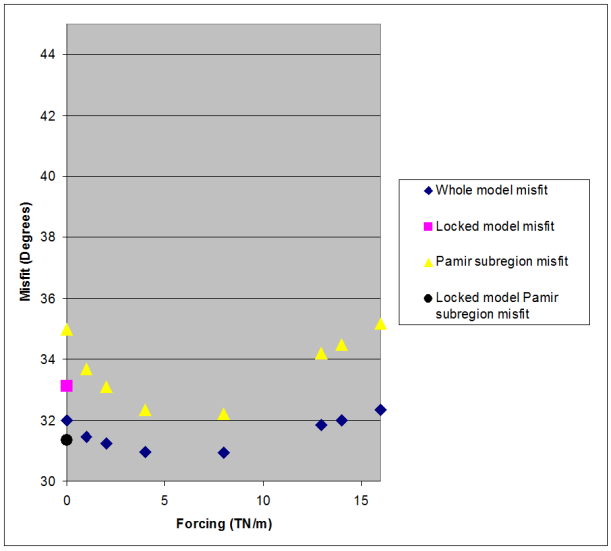

Figure 10: (a): The model and Pamir subregion misfit plotted as function of the forcing on the Pamir fault, in the normal scenario. (b): The model and Pamir subregion misfit plotted as function of the forcing on the Pamir fault, in the reverse scenario. A forcing with a magnitude of 0 TN/m indicates that displacement on the fault is allowed as a consequence of the original stress field, in contrast to the locked model, where no displacement on the fault is allowed. The data error ($\widehat{\Delta\beta}$) for the whole model and the Pamir subregion is $\pm 24^{\circ}$, the model averaging error ($\widehat{\Delta\zeta}$) for the whole model is $\pm\ 2^{\circ}$ and for the Pamir subregion $\pm\ 1^{\circ}$. The total uncertainty ($\widehat{\Delta\alpha}$) is $\pm\ 23^{\circ}$in both cases.

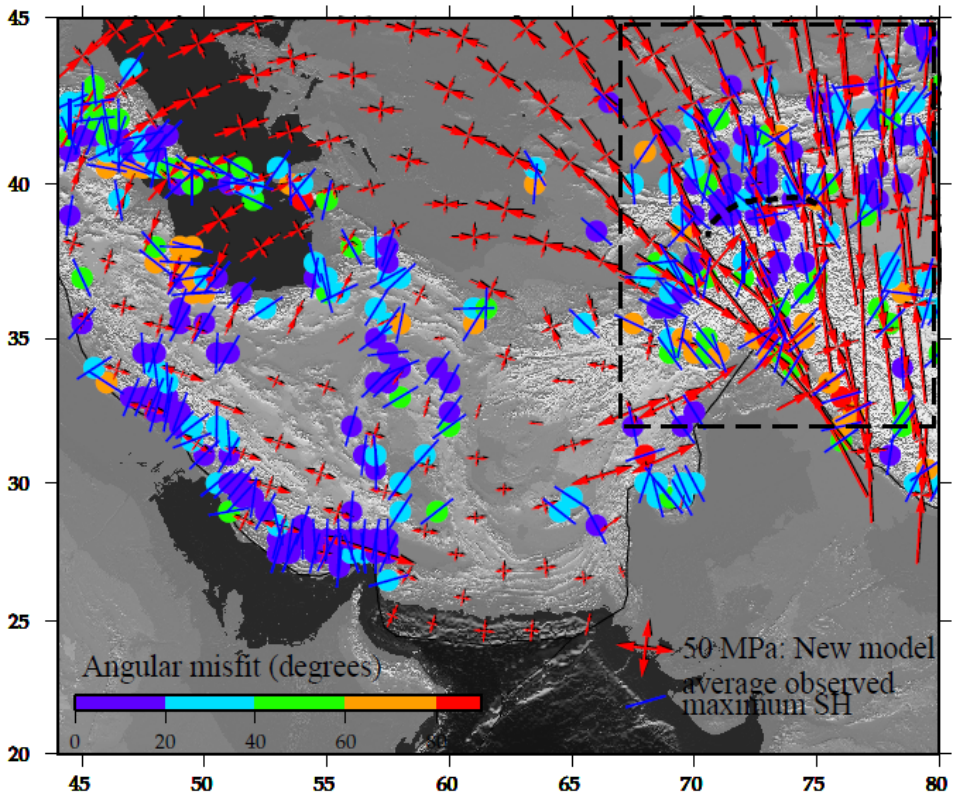

Figure 11: The stress field based on the observations collected by the WSM project compared to the stress field constructed using model *INdynabest*.

(a) Locked model

(b) Model *Kinebest*

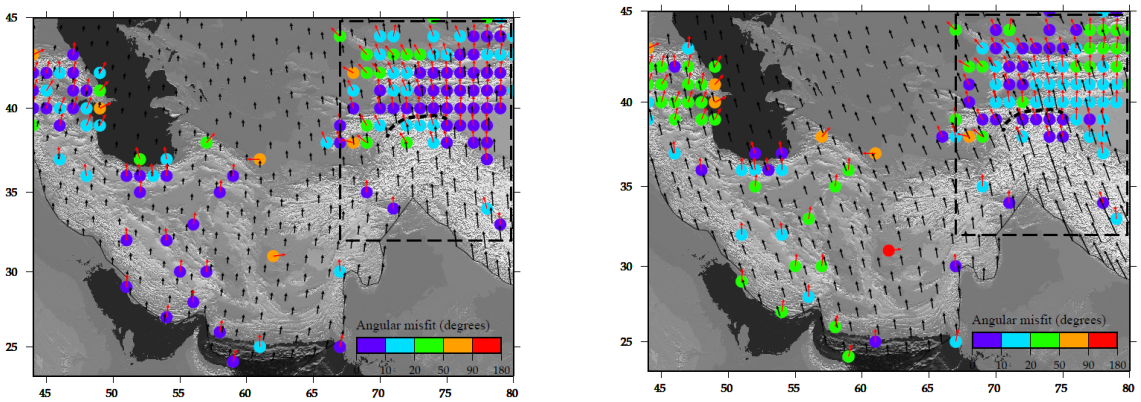

Figure 12: The relative displacement (black arrows) wrt to a fixed Eurasian plate which occurs in the locked model (left) and in model *Kinebest* (right) as a consequence of the imposed tractions. Circles in the background indicate the misfit in direction between the averaged displacement directions and the averaged observed velocity directions.

(a) Normal scenario

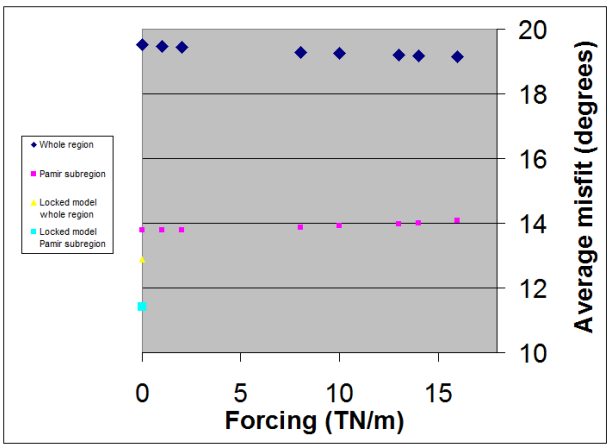

(b) Reverse scenario

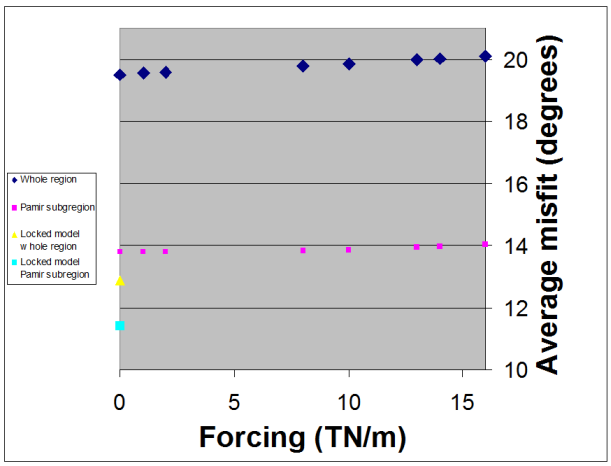

Figure 13: The displacement as a function of forcing on the slab for the normal, reverse and locked scenarios. Results include both the whole model and the Pamir subregion. The total uncertainty ($\widehat{\Delta\alpha}$) of all the data in these graphs is between 3.5 and 4.0˚. These graphs show that the misfit is fairly insensitive to the forcing on the slab

.

4.3 Displacements

In the work by WR the kinematics of the region were not included and these results cannot be benchmarked.

The comparison between modelled displacements as found in the locked model and observations can be found in figure 12a, which shows the directions and magnitudes of the modelled displacement and the directions of the observed velocities, as well as the misfit between the directions of these vectors. The average misfit between the modelled displacements and the observed velocities throughout the whole region is 12 ± 3.7° but most misfits are smaller than 5°.

When forcing on the Pamir fault is added to the model, the results in fit between modelled and observed displacement directions show a marked decrease. In all scenarios, the misfit between observations and model results are greater than 19 ± 3.8 degrees (see figure 13 which shows the misfit between modelled and observed directions). The average misfit between observed and modelled displacement directions appears fairly insensitive to the magnitude and directions of forcing. As such, the difference between the models is minimal, but the best fit for the whole region is obtained with maximum forcing in the initial scenario, which will be referred to as model *Kinebest*. The results of this model are mapped in figure 12b. In this scenario the fit in direction increases in the western Pamir region, but decreases everywhere else.

5 Analysis

We have presented four different model results which all have their stronger and weaker points. In this section, all models will be evaluated and compared with observations to determine which model is most representative. For reference, an overview of the results of the locked model and the models *Kinebest*, *EUDynabest* and *INDynabest* is presented in table 2.

Table 2: Model overview

	locked model	*Kinebest*	*EUdynabest*	*INdynabest*
Forcing (TN/m)	-	16	0	-8
Stress misfit (°)	33.1 ± 23.1	35.3 ± 23.7	32.0 ± 23.3	30.9 ± 23.5
Velocity misfit (°)	12.9 ± 3.7	19.1 ± 3.9	19.5 ± 3.7	19.8 ± 3.7

5.1 The locked model

The locked model gives the best results for displacement fits and reasonably good fits for the stress field. The main argument against this model is the nature of the current velocity field in the Pamir zone, with a velocity contrast between both sides of the fault (figure 1b). This could either be through large internal deformation or internal faulting. An increased resolution of the velocity field on both sides of the fault can provide clarity to this issue. Structural geological reconstructions of the region (Burtman and Molnar, 1993) show that although significant internal shortening has occurred, not all shortening can be accommodated through internal shortening alone. This implies the fault is still active and not 'locked' as in this model.

5.2 Model *INDynabest*

The model *INDynabest* gives the best results for stress field fits and is similar to the other active faulting models in displacement fit. However, since the slab has a dip to the south it is very unlikely that a northward pull can be exerted by this slab and that makes this scenario purely hypothetical.

5.3 Model *Kinebest*

The displacement results of this model are close to those of *EUDynabest* but the stress fits are vastly inferior to that model and so this model is discarded in favour of *EUDynabest*.

5.4 Model *EUDynabest*

The stress results of this model match those of the locked model rather closely, while the displacement results only show an improvement in the north-western Pamir region, but a sharp decrease in fit elsewhere. The forcing on this model is 0 TN/m which implies a perfect neutrally buoyant slab. This in turn implies subduction of buoyant crustal material, which will be further discusses in the next section.

6 Discussion

6.1 Model set-up

The results of the locked model match the results produced by WR fairly well and as such the model can be assumed benchmarked. This indicates that the boundary conditions representing the forces outside the modelling domain are dynamically consistent and should produce fairly accurate results. For the models that include an active pull on the Pamir fault zone a new set of boundary conditions is implemented.

Regarding the forcing on the fault zone assumptions on parameters which will strongly influence the results (the viscous resistance, the compositional buoyancy, frictionless contact and the thermal expansion coefficient in particularly) had to be made. For these parameters we have chosen values that can be considered an upper bound, so an optimal contrast could be obtained between a neutrally buoyant scenario and the scenario with maximal forcing. This definitely results in an overestimate, since for example numerical calculations based on differential equations (Turcotte and Schubert, 2002) show that the viscous resistance alone could be well over 10 TN/m (Burght van den, 2012). However, it has the advantage that the 'real' scenario falls within the upper and lower bounds of the models. A posteriori we can say that these boundary conditions do not affect the conclusion of the paper since our preferred model *EUdynabest* is on the lower bound of our model range.

Despite the fact that the model *EUdynabest* is not influenced by our choice of slab parameters, its results still deviate from the observations, indicating that other more basic assumptions may be flawed. The simplified geometry might be one of the factors that have an influence on the accuracy of the results. A lack of associated faults in the region (see fig. 1a), the (possible) pull on the slab underneath the Hindu Kush mountains (Koulakov and Sobolev, 2006; Sippl et al., 2013b) or the assumption of a lithosphere of uniform thickness Conrad and Lithgow-Bertelloni (2006); Naliboff et al. (2012) are all simplifications which will affect the stress field on the scale we are interested in. The set-up of the model is another factor which needs to be taken into account. Convergence is not tested when the Pamir fault is included and hence refining the mesh might provide different results. A purely elastic approach might not accurately represent a process as subduction and so including elasto-plastic properties (as for example used by Erickson and Jamison (1995)) or damage properties (Hieronymus et al., 2008; Guimaraes et al., 2009) will provide more insight in the nature of subduction zone.

6.2 Results

In most studies where the stress field is modelled the forcing components only include the LBF's, mantle tractions and edge forces. Including fault zones within the modelled domain is, with a few exceptions (Warners-Ruckstuhl et al., 2013; Koptev et al., 2010), not common practice. Where Warners-Ruckstuhl et al. (2013) found that including strike slip faults did not significantly alter the modelled stress field, our results show that including fault zones can influence the regional stress field to a certain degree (f.e. figure 10a) and hence for reproducing the stress field at greater resolution it will be essential to add local tectonic features.

The best model results are obtained in a setting of subduction of continental material of Eurasian origin, which gives the slab a neutral buoyancy. The neutral buoyancy is unexpected, since crustal material will turn to eclogite (which has a negative buoyancy (Cloos, 1993)) at pressure in excess of 1.9 GPA (>70 km depth) and temperatures over 600°C (Wang and Liou, 1991; Franz et al., 2001). In a subduction zone this pressure is reached at every point and so to maintain its positive buoyancy the crustal material should only reach high temperatures after extended periods of time. This is partially confirmed by a seismic interpretation by Schneider et al. (2013), where seismic velocity contrasts associated with non-eclogitized crust decrease from 100 km depth onwards but still occur at depths of at least 150 km, indicating that up to this depth the eclogitization process has not been completed yet.

If traces of the slab can be found to at least 300 km depth this still leaves 150 km of slab where the crust has turned to eclogite. A possible solution to this is delamination as proposed by Sippl et al. (2013a): the upper part of the slab consists of underthrusted continental material with a low density, whereas the mantle material with (partially) eclogitized crust delaminates and sinks to greater depths. The requirements for initiation of delamination of eclogitized crust and lithospheric mantle (the presence of fluids in the crustal material and a conduit between asthenospheric mantle and crustal material) as found by Krystopowicz and Currie (2013) are both present and so it is a real possibility that delamination occurs in this region. This delamination theory is further supported by earthquake data, which shows a gap in hypocentres at intermediate depths indicating an absence of crustal material. Tomography data sets generally show a continuous slab and so contradict slab detachment or delamination but this may be a resolution problem since for example the data sets of Koulakov and Sobolev (2006) show a slight increase in velocity in the regions without earthquake hypocentres. In the neighbouring Hindu Kush area an imaged thinning of the slab (Negredo et al., 2007) and sharp velocity contrast (Mellors et al., 1995) at 200 km depth indicates that a similar delamination process might be occurring here.

The consequence of the delamination process is that dense material in the lower slab is decoupled from the rest of the slab, allowing this upper part of the slab to maintain a neutral buoyancy and hence a low forcing on the lithosphere.

6.3 Implications: a case study of the Zagros region

The results from the Pamir modelling show that features of smaller wavelength than for example continental collision or mantle tractions may influence the stress field locally and regionally. In this section we will show the implications of this with the example of another debated issue: the possible occurrence of slab break-off in the Zagros.

The Zagros orogen is set in a similar setting as the Pamir region: on the boundary of two plates, in this case the Arabian and Eurasian plate, with a sharp velocity contrast (from 20 mm/y to 10 mm/y) across a main thrust fault in the region, as obtained from GPS (Vernant et al., 2004; Reilinger et al., 2006) and a more gradual decrease within the mountain belt itself. This sharp decrease indicates an active fault while the slower decrease within the Zagros region indicates internal deformation.

From seismic tomography and some gravity and geoid studies (Molinaro et al., 2005; Hafkenscheid et al., 2006; Paul et al., 2010; Agard et al., 2011; Mouthereau et al., 2012) it has been derived that slab break-off has occurred under parts of the Zagros. Although discussion about the exact timing and amount of break-off is still ongoing, most studies agree that slab break-off has occurred at least in the northwestern part of the Zagros and probably the central part as well over the last 12 Ma.

Recent slab break-off will have two important implications: mantle flow patterns and intensity will change and isostatic equilibrium is no longer obtained throughout the Zagros region. This latter is important since the lithospheric body forces are calculated with the assumption that the lithosphere is in isostatic equilibrium. The only way this could still be true after slab break-off is a vigorous flow to support the lithospheric columns dynamically, but such a scenario is unlikely to have arisen in a fairly short timespan. The consequence of the loss of isostatic equilibrium is that the GPE calculations are overestimates and hence the LBF's are probably overestimated as well. In both this study and the work done by WR the Zagros is assumed to be in isostatic equilibrium, which occurs for a continuous slab. The mantle flow is assumed to be a consequence of the slab break-off, since the upper 150 km of the mantle forcing is removed, and so the slab is represented as an unconnected dense body. This is internally contradictory and should be resolved by either assuming an intact slab and hence changing the mantle flow (most likely an increase in intensity due to both the presence of water and other lithospheric minerals (Billen, 2008) or the vigorous corner flow associated with subduction (Chapple and Tullis, 1977; Cavinato and Celles, 1999)) or by assuming a detached slab and recalculating the (presumably decreased) values of the LBF's.

The consequence of this alteration will undoubtedly be a new stress field in the Zagros region and by comparing resulting stress fields as is done in this study, an estimate can be made of the amount, if any, of the slab break-off that has occurred in this region, providing both insight in the processes occurring in and underneath the Zagros orogen and the nature of the lithospheric stress field.

7 Conclusions

From a discontinuity in the local GPS field we find that active faulting is taking place in the Pamir mountain belt. This faulting is associated to an ongoing subduction process. By modelling the stress field of the region using long-wavelength forcing and including forcing corresponding to a subduction process in the region, we then find that the best fit to the stress field for a realistic though simplified geometry is obtained for a neutrally buoyant slab. Therefore we conclude that active subduction of

buoyant continental material is occurring in the Pamir region.

8 Acknowledgements

The author would like to thank Rob Govers for supervision and discussions on the subject, Candela Garcia Lopez and Janneke van den Burght for assistance with the software. The author would also like to thank Paul Meijer, Nienke Blom and Ingrid Mulders for suggestions which improved the manuscript and Geertje ter Maat for assistance on the presentation of the subject.

Images are generated using the GMT toolset (Wessel and Smith, 1991).

Bibliography

P. Agard, J. Omrani, L. Jolivet, H. Whitechurch, B. Vrielynck, W. Spakman, P. Monié, B. Meyer, and R. Wortel. Zagros orogeny: a subduction-dominated process. *Geological Magazine*, 148(5-6):692–725, July 2011. ISSN 0016-7568. doi: 10.1017/S001675681100046X.

C. Amante and B. W. Eakins. ETOPO1 1 Arc-Minute Global Relief Model: Procedures, Data Sources and Analysis. *NOAA Technical Memorandum*, (March), 2009.

E. V. Artyushkov. Stresses in the lithosphere caused by crustal thickness inhomogeneities. *Journal of Geophysical Research*, 78(32): 7675–7708, November 1973. ISSN 01480227. doi: 10.1029/JB078i032p07675.

C. Bassin, G. Laske, and G. Masters. The Current Limits of Resolution for Surface Wave Tomography in North America. *Eos Trans. AGU*, 81, 2000.

V. V. Beloussov and N. A. Belyaevsky. Structure of the lithosphere along the deep seismic sounding profile: Tien ShanPamirsKarakorumHimalayas. *Tectonophysics*, 70:193–221, 1980.

M. I. Billen. Modeling the Dynamics of Subducting Slabs. *Annual Review of Earth and Planetary Sciences*, 36(1):325–356, May 2008. ISSN 0084-6597. doi: 10.1146/annurev.earth.36.031207.124129.

P. Bird. An updated digital model of plate boundaries. *Geochemistry, Geophysics, Geosystems*, 4(3), March 2003. ISSN 15252027. doi: 10.1029/2001GC000252.

K. T. Budanova. Metamorficheskie porody Tadzhikistana [Metamorphic formation of Tajikistan]. *Akademiya Nauk Tadzhikskoy SSR*, 1991.

J. C. H. Burght van den. *Dynamics of the Eurasian plate at 40 Ma: placing a dynamic constraint on lithosphere-mantle coupling*. PhD thesis, Utrecht university, 2012.

V. S. Burtman and P. Molnar. Geological and Geophysical Evidence for Deep Subduction of Continental Crust Beneath the Pamir. *The geological society of America*, (281), 1993.

G. P. Cavinato and P. G. De Celles. Extensional basins in the tectonically bimodal central Apennines fold-thrust belt, Italy: response to corner flow above a subducting slab in retrograde motion. *Geology*, 1999. doi: 10.1130/0091-7613(1999)027¡0955.

W. M. Chapple and T. E. Tullis. Evaluation of the forces that drive the plates. *Journal of geophysical research*, 82(14), 1977.

J. L. Chatelain, S. W. Roecker, D. Hatzfeld, and P. Molnar. Microerthquake seismicity and fault plane solution in the Hindu Kush Region and their tectonic implications. *Journal of Geophysical Research*, 85(3):1365–1387, 1980. doi: 10.1029/JB085iB03p01365.

M. Cloos. Lithospheric buoyancy and collisional orogenesis: Subduction of oceanic plateaus, continental margins, island arcs, spreading ridges, and seamounts. *Geological Society of America Bulletin*, 105(6):715, 1993. ISSN 0016-7606.

C. P. Conrad and C. Lithgow-Bertelloni. Influence of continental roots and asthenosphere on plate-mantle coupling. *Geophysical Research Letters*, 33(5):2–5, 2006. ISSN 0094-8276. doi: 10.1029/2005GL025621.

C. DeMets, R. G. Gordon, D. F. Argus, and S. Stein. Effect of recent revisions to the geomagnetic reversal time scale on estimates of current plate motions. *Geophysical research letters*, 21(20):2191–2194, 1994.

M. N. Ducea, V. Lutkov, V. T. Minaev, B. Hacker, L. Ratschbacher, P. Luffi, M. Schwab, G. E. Gehrels, M. McWilliams, J. Vervoort, and J. Metcalf. Building the Pamirs: The view from the underside. *Geology*, 31(10):849, 2003. ISSN 0091-7613. doi: 10.1130/G19707.1.

P. England and R. Wortel. Some consequences of the subduction of young slabs. *Earth and Planetary Science Letters*, 47:403–415, 1980.

S. G. Erickson and W. R. Jamison. Viscous-plastic finite-element models of fault-bend folds. *Journal of Structural Geology*, 17(3), 1995.

G. Fan, J. F. Ni, and T. C. Wallace. Active tectonics of the Pamirs and Karakorum. *Journal of Geophysical Research: Solid Earth*, 99: 7131–7160, 1994. doi: 10.1029/93JB02970.

D. Forsyth and S. Uyeda. On the Relative Importance of the Driving Forces of Plate Motion*. *Geophysical Journal of the Royal Astronomical Society*, (2241), 1975.

L. Franz, R. L. Romer, R. Klemd, R. Schmid, R. Oberhänsli, T. Wagner, and D. Shuwen. Eclogite-facies quartz veins within metabasites of the Dabie Shan (eastern China): pressure-temperature-time-deformation path, composition of the fluid phase and fluid flow during exhumation of high-pressure rocks. *Contributions to Mineralogy and Petrology*, 141(3):322–346, June 2001. ISSN 0010-7999. doi: 10.1007/s004100000233.

S. M. Gordon, P. Luffi, B. Hacker, J. Valley, M. Spicuzza, R. Kozdon, P. Kelemen, L. Ratshbacher, and V. Minaev. The thermal structure of continental crust in active orogens: insight from Miocene eclogite and granulite xenoliths of the Pamir Mountains. *Journal of Metamorphic Geology*, 30(4):413–434, May 2012. ISSN 02634929. doi: 10.1111/j.1525-1314.2012.00973.x.

R. Govers and P. Th. Meijer. On the dynamics of the Juan de Fuca plate. *Earth and Planetary Science Letters*, 189(3-4):115–131, July 2001. ISSN 0012821X. doi: 10.1016/S0012-821X(01)00360-0.

S. P. Grand. Mantle shearwave tomography and the fate of subducted slabs. *Philosophical Transactions: Mathematical, Physical and Engineering Sciences*, 360(1800):2475–2491, 2002.

S. Guillot, E. Garzanti, D. Baratoux, D. Marquer, G. Mahéo, and J. de Sigoyer. Reconstructing the total shortening history of the NW Himalaya. *Geochemistry, Geophysics, Geosystems*, 4(7), July 2003. ISSN 15252027. doi: 10.1029/2002GC000484.

L. Guimaraes, I. F. Gomes, and J. P. V. Fernandes. Influence of Mechanical Constitutive Model on the Coupled Hydro Geomechanical Analysis of Fault Reactivation. *SPE Reservoir Simulation Symposium*, 2009.

E. Hafkenscheid, M. J. R. Wortel, and W. Spakman. Subduction history of the Tethyan region derived from seismic tomography and tectonic reconstructions. *Journal of Geophysical Research*, 111(B8):B08401, 2006. ISSN 0148-0227. doi: 10.1029/2005JB003791.

M. W. Hamburger, D. R. Sarewitz, L. Pavlis, and G. A. Popandopulo. Structural and seismic evidence for intracontinental subduction in the Peter the First Range, central Asia. *Geological Society of America Bulletin*, 104(4):397–408, 1992.

O. Heidbach, M. Tingay, A. Barth, J. Reinecker, D. Kurfeß, and B. Müller. The world stress map database release 2008. Technical report, 2008.

C. F. Hieronymus, S. Goes, M. Sargent, and G. Morra. A dynamical model for generating Eurasian lithospheric stress and strain rate fields: Effect of rheology and cratons. *Journal of Geophysical Research*, 113(B7):B07404, July 2008. ISSN 0148-0227. doi: 10.1029/2007JB004953.

D. J. J. Hinsbergen, van, P. Kapp, G. Dupont-Nivet, P. C. Lippert, P. G. DeCelles, and T. H. Torsvik. Restoration of Cenozoic deformation in Asia and the size of Greater India. *Tectonics*, 30(5), October 2011. ISSN 02787407. doi: 10.1029/2011TC002908.

C. T. Klootwijk, J. S. Gee, J. W. Peirce, G. M. Smith, and P. L. McFadded. An early India-Asia contact: paleomagnetic constraints from Ninetyeast Ridge, ODP leg 121. *Geology*, 20:395–398, 1992. doi: 10.1130/0091-7613(1992)020¡0395.

A. Koptev, A. Ershov, and O. Levchenko. Numerical modeling of lithospheric stress field and buckling in the Indian ocean. *EGU General Assembly*, 12:14199, 2010.

I. Koulakov and S. V. Sobolev. A tomographic image of Indian lithosphere break-off beneath the Pamir-Hindukush region. *Geophysical Journal International*, 164(2):425–440, February 2006. ISSN 0956540X. doi: 10.1111/j.1365-246X.2005.02841.x.

N. J. Krystopowicz and C. A. Currie. Crustal eclogitization and lithosphere delamination in orogens. *Earth and Planetary Science Letters*, 361:195–207, January 2013. ISSN 0012821X. doi: 10.1016/j.epsl.2012.09.056.

W. Leith and W. Alvarez. Structure of the Vakhsh fold-and-thrust belt, Tadjik SSR: Geologic mapping on a Landsat image base. *Geological Society of America*, (July):875–885, 1985.

A. A. Lukk, S. L. Yunga, V. I. Shevchenko, and M. W. Hamburger. Earthquake focal mechanisms, deformation state, and seismotectonics of the PamirTien Shan region, Central Asia. *Journal of Geophysical Research: Solid Earth*, 100, 1995.

K. V. Mardia. *Statistics of Directional Data*. Academic Press, London, 1972.

M. Mattauer. Intracontinental subduction, crust-mantle decollement and crustal-stacking wedge in the Himalayas and other collision belts. *Geological Society, London, Special Publications*, 19(1):37–50, January 1986. ISSN 0305-8719. doi: 10.1144/GSL.SP.1986.019.01.02.

D. P. McKenzie. Speculations on the consequences and causes of plate motions. *Geophysical Journal International*, (1608):1–32, 1969.

J. Mechie, X. Yuan, B. Schurr, F. Schneider, C. Sippl, L. Ratschbacher, V. Minaev, M. Gadoev, I. Oimahmadov, U. Abdybachaev, B. Moldobekov, S. Orunbaev, and S. Negmatullaev. Crustal and uppermost mantle velocity structure along a profile across the Pamir and southern Tien Shan as derived from project TIPAGE wide-angle seismic data. *Geophysical Journal International*, 188(2):385–407, February 2012. ISSN 0956540X. doi: 10.1111/j.1365-246X.2011.05278.x.

R. J. Mellors, G. L. Pavlis, M. W. Hamburger, H. J. Al-Shukri, and A. A. Lukk. Evidence for a high-velocity slab associated with the Hindu Kush seismic zone. *Journal of Geophysical Research*, 100(B3):4067, 1995. ISSN 0148-0227. doi: 10.1029/94JB02642.

H. J. Melosh and C. A. Williams. Mechanics of graben formation in crustal rocks: A finite element analysis. *Journal of Geophysical Research: Solid Earth*, 94, 1989.

K. Milner, T. W. Becker, L. Boschi, J. Sain, D. Schorlemmer, and H. Waterhouse. The Solid Earth Research and Teaching Environment: a new software framework to share research tools in the classroom and across disciplines. *Eos Trans. AGU*, 90(12):2009, 2009.

J. X. Mitrovica and A. M. Forte. A new inference of mantle viscosity based upon joint inversion of convection and glacial isostatic adjustment data. *Earth and Planetary Science Letters*, 225(1-2):177–189, August 2004. ISSN 0012821X. doi: 10.1016/j.epsl.2004.06.005.

S. Mohadjer, R. Bendick, A. Ischuk, S. Kuzikov, A. Kostuk, U. Saydullaev, S. Lodi, D. M. Kakar, A. Wasy, M. A. Khan, P. Molnar, R. Bilham, and A. V. Zubovich. Partitioning of India-Eurasia convergence in the Pamir-Hindu Kush from GPS measurements. *Geophysical Research Letters*, 37(4), February 2010. ISSN 00948276. doi: 10.1029/2009GL041737.

M. Molinaro, H. Zeyen, and X. Laurencin. Lithospheric structure beneath the south-eastern Zagros Mountains, Iran: recent slab break-off? *Terra Nova*, 17(1):1–6, February 2005. ISSN 0954-4879. doi: 10.1111/j.1365-3121.2004.00575.x.

P. Molnar and H. Lyon-Caen. Some simple physical aspects of the support, structure and evolution of mountain belts. *Geological society of America*, 218:179–209, 1988.

F. Mouthereau, O. Lacombe, and J. Vergés. Building the Zagros collisional orogen: Timing, strain distribution and the dynamics of Arabia/Eurasia plate convergence. *Tectonophysics*, 532-535:27–60, April 2012. ISSN 00401951. doi: 10.1016/j.tecto.2012.01.022.

J. B. Naliboff, C. Lithgow-Bertelloni, L. J. Ruff, and N. de Koker. The effects of lithospheric thickness and density structure on Earth's stress field. *Geophysical Journal International*, 188(1):1–17, January 2012. ISSN 0956540X. doi: 10.1111/j.1365-246X.2011.05248.x.

A. M. Negredo, A. Replumaz, A. Villaseñor, and S. Guillot. Modeling the evolution of continental subduction processes in the PamirHindu Kush region. *Earth and Planetary Science Letters*, 259(1-2):212–225, July 2007. ISSN 0012821X. doi: 10.1016/j.epsl.2007.04.043.

A. Paul, D. Hatzfeld, A. Kaviani, M. Tatar, and C. Pequegnat. Seismic imaging of the lithospheric structure of the Zagros mountain belt (Iran). *Geological Society, London, Special Publications*, 330(1):5–18, June 2010. ISSN 0305-8719. doi: 10.1144/SP330.2.

G. Pegler and S. Das. An enhanced image of the Pamir-Hindu Kush seismic zone from relocated earthquake hypocentres. *Geophysical Journal International*, 134(2):573–595, August 1998. ISSN 0956540X. doi: 10.1046/j.1365-246x.1998.00582.x.

R. Reilinger, S. McClusky, P. Vernant, S. Lawrence, S. Ergintav, R. Cakmak, H. Ozener, F. Kadirov, I. Guliev, R. Stepanyan, M. Nadariya, G. Hahubia, S. Mahmoud, K. Sakr, A. ArRajehi, D. Paradissis, A. Al-Aydrus, M. Prilepin, T. Guseva, E. Evren, A. Dmitrotsa, S. V. Filikov, F. Gomez, R. Al-Ghazzi, and G. Karam. GPS constraints on continental deformation in the Africa-Arabia-Eurasia continental collision zone and implications for the dynamics of plate interactions. *Journal of Geophysical Research*, 111(B5):B05411, 2006. ISSN 0148-0227. doi: 10.1029/2005JB004051.

D. Richter and G. Simmons. Thermal expansion behavior of igneous rocks. *International Journal of Rock Mechanics and Mining Sciences & Geomechanics Abstracts*, 11(10):403–411, October 1974. ISSN 01489062. doi: 10.1016/0148-9062(74)91111-5.

S. W. Roecker. Velocity structure of the PamirHindu Kush Region: Possible evidence of subducted crust. *Journal of Geophysical Research: Solid Earth*, 87:945–959, 1982.

F. M. Schneider, X. Yuan, B. Schurr, J. Mechie, C. Sippl, C. Haberland, V. Minaev, I. Oimahmadov, M. Gadoev, N. Radjabov, U. Abdybachaev, S. Orunbaev, and S. Negmatullaev. Seismic imaging of subducting continental lower crust beneath the Pamir. *Earth and Planetary Science Letters*, 375:101–112, August 2013. ISSN 0012821X. doi: 10.1016/j.epsl.2013.05.015.

M. Searle, B. R. Hacker, and R. Bilham. The Hindu Kush Seismic Zone as a Paradigm for the Creation of UltrahighPressure Diamondand CoesiteBearing Continental Rocks. *The Journal of Geology*, 109:143–153, 2001.

J. R. Shewchuk. Triangle: Engineering a 2D Quality Mesh Generator and Delaunay Triangulator. *Lecture Notes in Computer Science*, 1448:203–222, 1996.

N. A. Simmons, A. M. Forte, and S. P. Grand. Joint seismic, geodynamic and mineral physical constraints on three-dimensional mantle heterogeneity: Implications for the relative importance of thermal versus compositional heterogeneity. *Geophysical Journal International*, 177(3):1284–1304, June 2009. ISSN 0956540X. doi: 10.1111/j.1365-246X.2009.04133.x.

C. Sippl, B. Schurr, and F. Schneider. A two-step underthrusting and delamination model that explains deep structures beneath Pamir and Hindu Kush. *Geophysical Research Abstracts*, 2013a.

C. Sippl, B. Schurr, and X. Yuan. Geometry of the Pamir-Hindu Kush intermediate-depth earthquake zone from local seismic data. *Journal of Geophysical Research*, 118:1–20, 2013b. doi: 10.1002/jgrb.50128.

E. R. Sobel and T. A. Dumitru. Thrusting and exhumation around the margins of the western Tarim basin during the India-Asia collision. *Journal of Geophysical Research*, 102(96):5043–5063, 1997.

E. R. Sobel, L. M. Schoenbohm, J. Chen, R. Thiede, D.F. Stockli, M. Sudo, and M. R. Strecker. Late MiocenePliocene deceleration of dextral slip between Pamir and Tarim: Implications for Pamir orogenesis. *Earth and Planetary Science Letters*, 304(3-4):369–378, April 2011. ISSN 0012821X. doi: 10.1016/j.epsl.2011.02.012.

C. A. Stein and S. Stein. A model for the global variation in oceanic depth and heat flow with lithospheric age. *Nature*, 358:123–128, 1992.

C. Sung and R. G. Burns. Kinetics of high-pressure phase transformations: Implications to the evolution of the olivine spinel transition in the downgoing lithosphere and its consequences on. *Tectonophysics*, 31, 1976.

D. L. Turcotte and G. Schubert. *Geodynamics*. Cambridge University Press, 2002.

Ph. Vernant, F. Nilforoushan, D. Hatzfeld, M. R. Abbassi, C. Vigny, F. Masson, H. Nankali, J. Martinod, A. Ashtiani, R. Bayer, F. Tavakoli, and J. Chéry. Present-day crustal deformation and plate kinematics in the Middle East constrained by GPS measurements in Iran and northern Oman. *Geophysical Journal International*, 157(1):381–398, April 2004. ISSN 0956540X. doi: 10.1111/j.1365-246X.2004.02222.x.

X. Wang and J. G. Liou. Regional ultrahigh-pressure coesite-bearing eclogitic terrane in central China: Evidence from country rocks, gneiss, marble, and metapelite. *Geology*, 1991. doi: 10.1130/0091-7613(1991)019¡0933.

K. N. Warners-Ruckstuhl, R. Govers, and M. J. R. Wortel. Tethyan collision forces and the stress field of the Eurasian Plate. *Geophysical Journal International*, June 2013. ISSN 0956-540X. doi: 10.1093/gji/ggt219.

P. Wessel and W. H. F. Smith. Free software helps map and display data. *Eos, Transactions American Geophysical Union*, 72(41):441–441, 1991. ISSN 0096-3941. doi: 10.1029/90EO00319.

T. Wong and W. F. Brace. Thermal expansion of rocks: Some measurements at high pressure. *Tectonophysics*, 57:95–117, 1979.

J. Zhang, X. Shan, and X. Huang. Seismotectonics in the Pamir: An oblique transpressional shear and south-directed deep-subduction model. *Geoscience Frontiers*, 2(1):1–15, January 2011. ISSN 16749871. doi: 10.1016/j.gsf.2010.11.002.

A. V. Zubovich, X. Wang, Y. G. Scherba, G. G. Schelochkov, R. Reilinger, C. Reigber, O. I. Mosienko, P. Molnar, W. Michajljow, V. I. Makarov, J. Li, S. I. Kuzikov, T. A. Herring, M. W. Hamburger, B. H. Hager, Y. Dang, V. D. Bragin, and R. T. Beisenbaev. GPS velocity field for the Tien Shan and surrounding regions. *Tectonics*, 29(6), December 2010. ISSN 02787407. doi: 10.1029/2010TC002772.

Appendices

A Calculation and comparison of the boundary conditions

In this appendix the calculation of each set of nodal forces (mantle tractions, LBF's, edge forces) will be explained in some detail. The final nodal point force value is determined through three steps. For nodes which lie at the predefined boundaries, only the boundary condition forces as derived from the results from WR are defined. On all other nodes the forces as a consequence of mantle tractions and LBF's are set. Nodes on the remaining boundary get an additional forcing which is the consequence from mechanical interaction between plates.

A.1 GPE forces and mantle tractions

After obtaining the topography data from the ETOPO1 set, the topography data is averaged of 2x2° (120 by 120 arcminute) cells using a standard averaging approach:

$$h_{av} = \frac{\sum_{x=1,y=1}^{x=120,y=120} h(x,y)}{x_{max} \cdot y_{max}} \tag{2}$$

where h_{av} is the average topography, $h(x,y)$ is the topography at location x,y and x_{max} and y_{max} correspond to the maximum value for x and y (120). The crustal thicknesses in the CRUST2.0 dataset are divided into 7 distinct layers with corresponding crustal densities. The thickness of the crust in a cell is calculated through

$$h_c = \sum_{n=1}^{7} h(n) \tag{3}$$

where h_c is the crustal thickness and h(n) is the thickness of the n-th layer. The average density (ρ_c) of this layer is then calculated through

$$\rho_c = \frac{\sum_{n=1}^{7} h(n) \cdot \rho(n)}{h_c} \tag{4}$$

The lithospheric body forces and their corresponding gradients can be described by

$$F_x = \frac{\Delta}{\Delta x} P, \quad F_y = \frac{\Delta}{\Delta y} P \tag{5}$$

where P is the lithostatic pressure calculated through

$$P = \int_{L}^{-h} \left(\int_{z}^{L} \rho(z')\ g\ dz' \right) dz \tag{6}$$

Here F_x and F_y are the perpendicular horizontal components of the traction (N/m^2) generated by the geopotential energy (GPE) P (N/m), ρ is the average lithospheric density (kg/m^3) dependent on depth z', g the acceleration due to the gravitational force (m/s^2), z is the depth (m) with z=0 at sealevel, h is the topography (m) and L is the total depth (m). Since the results from mantle flow modelling in this study are acquired assuming a lithospheric thickness of 100 km, the value for L for

Table 3: Reference values for the calculations of the lithostatic pressure

Parameter	**symbol**	**value**
Crustal density	ρ_{cref}	2850 kg/m^3
Crustal thickness	h_{cref}	35 km
Maximum lithospheric depth	L	100 km
Seawater density	ρ_w	1000 kg/m^3
Gravitational acceleration	g	9.81 m/s^2

these calculations will be set at the same value.

A reference lithospheric column is defined using the values found in table 3 and zero mantle tractions. Lithospheric columns using the values of equations (4) and (3) are compared with this column and from this we can find the lithospheric mantle density through

$$\rho_m = \frac{\rho_{cref} h_{cref} + \rho_{avref}(L - h_{cref}) + \tau_m/g - \rho_{cr} h_{cr}}{L + h - h_{cr}} \tag{7}$$

for positive topography and

$$\rho_m = \frac{\rho_{cref} h_{cref} + \rho_{avref}(L - h_{cref}) + \tau_m/g - \rho_{cr} h_{cr} + \rho_w h}{L + h - h_{cr}} \tag{8}$$

for regions below sea level. In these equations ρ_m is the lithospheric mantle density (kg/m^3), τ_m the normal mantle traction (N/m^2), ρ_{cr} is the average crustal density obtained from CRUST2.0 (kg/m^3) and h_{cr} is the crustal thickness (m), also obtained from CRUST2.0.

Since the total lithospheric density is now constant, the integral from equation 6 can be written as

$$P = g(\frac{1}{2}\rho_{cr} h_{cr}^2 + \frac{1}{2}\rho_m (L + h - h_{cr})^2 + \rho_{cr}(L + h - h_{cr}) h_{cr}) \tag{9}$$

for positive topography and as

$$P = g(\frac{1}{2}\rho_{cr} h_{cr}^2 + \frac{1}{2}\rho_m (L + h - h_{cr})^2 + \rho_{cr}(L + h - h_{cr}) h_{cr} + \frac{1}{2}\rho_w h^2 - (L + h) h \rho_w) \tag{10}$$

for regions below sea level.

Using these values for P in equation 5, with $\frac{\Delta}{\Delta x}$ and $\frac{\Delta}{\Delta y}$ covering the distance between the centres of two 2x2° cells gives a first estimate of the horizontal force acting on that region. The values for P and the forces which arise as a consequence of the variations in P over a 1x1° grid can be found in figure 14.

Mantle tractions are derived from the Ngrand model (Grand, 2002) using the SEATREE interface (Milner et al., 2009) with a viscosity profile from Simmons et al. (2009) (see figure 14). When comparing these mantle tractions with the tractions used by WR, a difference in magnitude and direction can be observed. Since the magnitude in most of the modelled region is smaller by almost an order of magnitude compared to the GPE forces, it is a safe estimate that the influence of the mantle tractions on the final stress field is probably relatively small and the difference in mantle tractions should not alter the results significantly.

Both mantle tractions and GPE tractions are defined over a square 2x2° grid, but they need to be applied to a smaller triangular grid. This example will continue using the GPE tractions in the x-direction, but the approach for the mantle forces and the y-direction is identical. If a change from total magnitude and direction tot x- and y-components or vice versa is required, this is obtained through trigonometry. The first step is to derive the forces acting on the triangular elements. The

force acting on a triangular element (F_{Ex}) is calculated by:

$$F_{Ex} = \sum_{i=1}^{j} F_X(i) \cdot area(i) \tag{11}$$

Where area corresponds to the surface of the triangular element(m^2) inside square element i and F_X to the traction in the x-direction (N/m^2) acting on that square element. j is the number of square elements the triangle has overlap with. For all of the triangular elements it is checked whether their vertices (which are the nodes of finite element mesh) lie inside or on the edges of a 2x2° square element. If this is the case $i = 1$ and the area is calculated using

$$area = |x_1(y_2 - y_3) + x_2(y_3 - y_1) + x_3(y_1 - y_2)| \tag{12}$$

where x and y are the coordinates of the three vertices of the triangular element. If only 1 vertex of the triangular element is inside or on a square element, equation (12) is used again since in most cases the area will have a triangular shape, but in this case x_1 and y_1 correspond to the coordinates of the node which lies inside the square element and x_2, y_2, x_3 and y_3 correspond to the coordinates where the triangle intersects with square element. In this case j in equation (11) will be greater than 1. In the case that 2 vertices lie inside or on a square element, the area has a quadrilateral shape and the surface area is calculated using both Brahmagupta's theorem and the surface formula for a trapezoid. Both cases are unable to calculate the area precisely since the requirements for either[1] are not matched, but give a close approximation. After comparing the results, it was found that the area calculated Brahmagupta's equation represented the true area better and hence this theorem is used in all cases:

$$\begin{aligned} e &= \frac{a+b+c+d}{2} \\ area &= \sqrt{(e-a)\cdot(e-b)\cdot(e-c)\cdot(e-d)} \end{aligned} \tag{13}$$

where a, b, c and d are length of the sides of the quadrilateral, whose vertices are made up by the vertices of the triangular element which lie inside the square element and the vertices where triangular element intersects with the square element.

Combining these three cases with the grid density used in our model gave an area coverage of over 97%. It is fairly easy to think of the cases where the missing 2-3% come from (for example all three vertices are outside a square element, but there is still overlap), but to find working algorithms for those few exceptions is too time intensive for this study. Another way to increase the area coverage is to increase the grid density, but this will consequently increase the computational time of the models significantly.

After calculating the forces acting on the elements (F_{Ex}) the forces acting on the nodes (F_{Nx}) can be calculated, assuming that forcing is evenly distributed over the area of the elements.

$$F_{Nx} = \sum_{i=1}^{n} \frac{F_{Ex}(i)}{3} \tag{14}$$

where n is the number of elements which share this specific node. Combining the nodal forces in the x and y direction gives the total nodal forces.

[1]To use Brahmagupta's theorem it is required that all four vertices fall on the circumference of a circle, for a trapezoid it is required that the top and base are parallel.

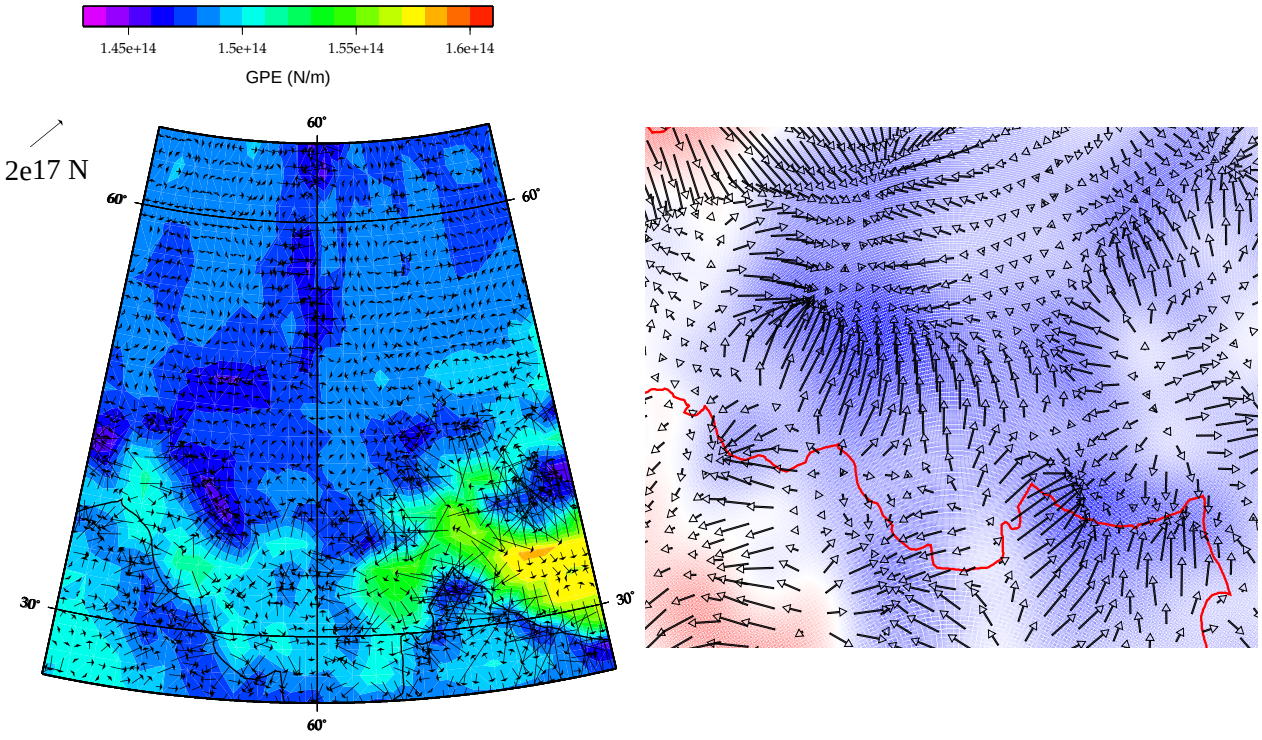

Figure 14: Left: the GPE as calculated using *Lithodens* and the associated Lithospheric Body Forces in a 1x1° grid. Right: the mantle tractions as derived from nGrand (Grand, 2002). Blue colours indicate downwellings, red colours indicate upwellings. The mantle tractions are on average one order of magnitude smaller than the GPE tractions. Both mantle tractions and LBF's are converted to nodal point forces used to constrain the stress field in the model.

A.2 Boundary forces

The forcing along the predefined boundaries is obtained by calculating the tractions on these boundaries from the stress field as calculated by WR. Using Cauchy's theorem the stress tensors (σ_{ij}) acting on the boundary nodes are converted to tractions $T_j^{(n)}$.

$$T_j^{(n)} = \sigma_{ij} n_i \tag{15}$$

These tractions are then multiplied by the thickness of the elements and length covered by a node as calculated by

$$length = \frac{\sqrt{(x_{i-1} - x_i)^2 + (y_{i-1} - y_i)^2}}{2} + \frac{\sqrt{(x_i - x_{i+1})^2 + (y_i - y_{i+1})^2}}{2} \tag{16}$$

where x_i and y_i are the x and y coordinates of the node considered and the other coordinates are the coordinates of its nearest neighbours on either side. The forces corresponding to the stress tensors obtained from the model by WR can be found in figure 15. Along the eastern boundary the tractions do not seem to correspond to the associated stresses very well. However, the stress field along most of this boundary is highly irregular and since only a few stress results have been picked to base the boundary conditions on, these few points may not give an accurate representation. The biggest misfit appears to the north-east. Since this is far from the region of interest, this is not expected to degenerate the results much.

The magnitudes of the tractions of the continental collision forces are obtained from WR and the directions are taken anti-parallel to the direction of plate motion as defined by NUVEL 1A (DeMets et al., 1994). The tractions are again multiplied by the length found by equation (16). The resulting nodal forces can be found in figure 15.

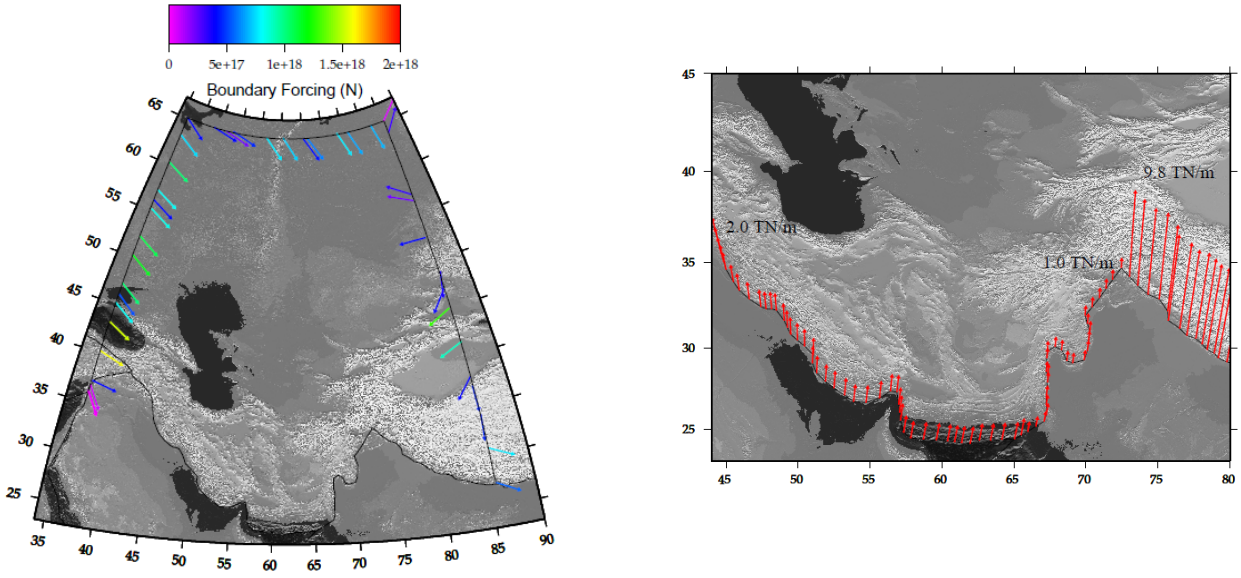

Figure 15: Left: the nodal forces obtained through the stresses found by WR. Right: the nodal forces representing the collision of India and Arabia with Eurasia.

A.3 Pamir pull

The Pamir fault itself is modelled using slippery nodes (Melosh and Williams, 1989). Elements sharing slippery nodes can move relative to one another without creating gaps in the mesh. In the case of the Pamir fault both strike-slip and thrust components of movement need to be accounted for and so two degrees of freedom are allowed for. As a consequence of the properties of slippery nodes, the elements that are on the overriding part of the mesh will not directly be influenced by the forcing on the subducting plate. Since the forcing calculated in section 3.3.3 is only the upper bound, several models are tested with different forcing on the Pamir fault zone.

Every element that shares a slippery node needs to be assigned a value that defines it as a part of either the overriding plate (for which we have chosen a positive value) or subducting plate (negative value). Since on every slippery node displacement is allowed, this effectively means that the fault needs to be bound by one normal node on either side of the fault, and that elements sharing this node and a slippery node need to be assigned a defining value as well. The results can be viewed in figure 16. The next step is to assign the correct forcing to the slippery nodes. The forcing as calculated in section 3.3.3 is added perpendicular to the orientation of the fault on the slippery nodes. The nodal point force magnitude is calculated in the same way as the magnitude of the forcing on the southern boundaries was calculated. The direction was assumed to be perpendicular to the orientation of the fault. The direction and magnitude of forcing for the upper limit case can be found in figure 16. For the models where the under- and overthrusting plate are interchanged, the direction of the forcing is rotated by 180 degrees.

A.4 Anchor points and associated stresses

A requirement of the modelling software to obtain accurate results is that at least two of the mesh nodes have an imposed boundary condition of zero displacement. Since the whole of the modelled domain is moving, this means that model results around these node will be severely distorted, since zero displacement requires a very high stress acting on the specific nodes. This problem has been partially circumvented by using nodal Winkler forces and by placing the anchor points in the region where displacement of the model is the smallest. Nodal Winkler forces act as a spring on the mesh,

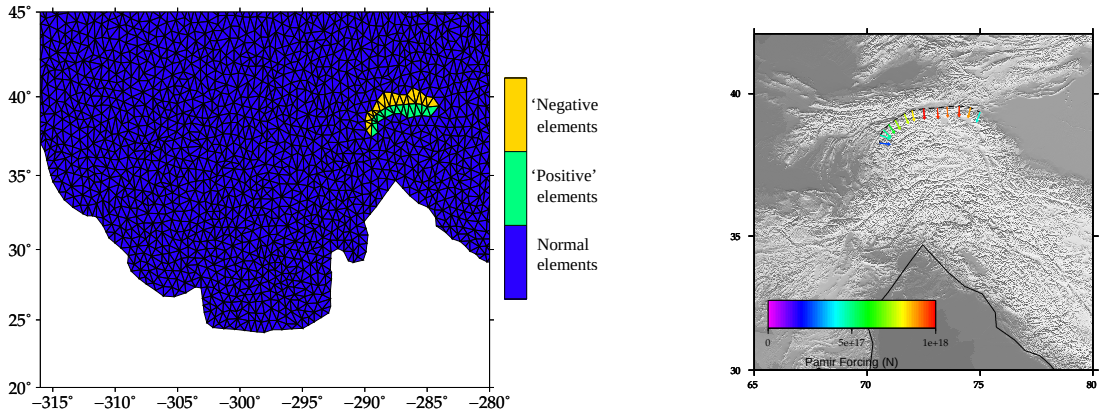

Figure 16: Left: Part of the mesh with slippery elements indicated in different colours. Right: the nodal forces for the 16 TN/m Eurasian subduction scenario. Note that in this case the forces act only on the yellow elements of the left figure.

so that if there is forcing on a node due to the model conditions, an opposite oriented force will act on the node as well. This does not influence the stress field, but it does decrease the displacement of the mesh, making it easier to apply the zero displacement boundary conditions. After applying the nodal Winkler forces, the anchor points have been placed at several locations in the mesh and tested for their influence. As can be seen in figure 17 the best location is in the upper left corner of the mesh, since the displacement is relatively small here independent of the location of the anchor points and it is located far away from our region of interest.

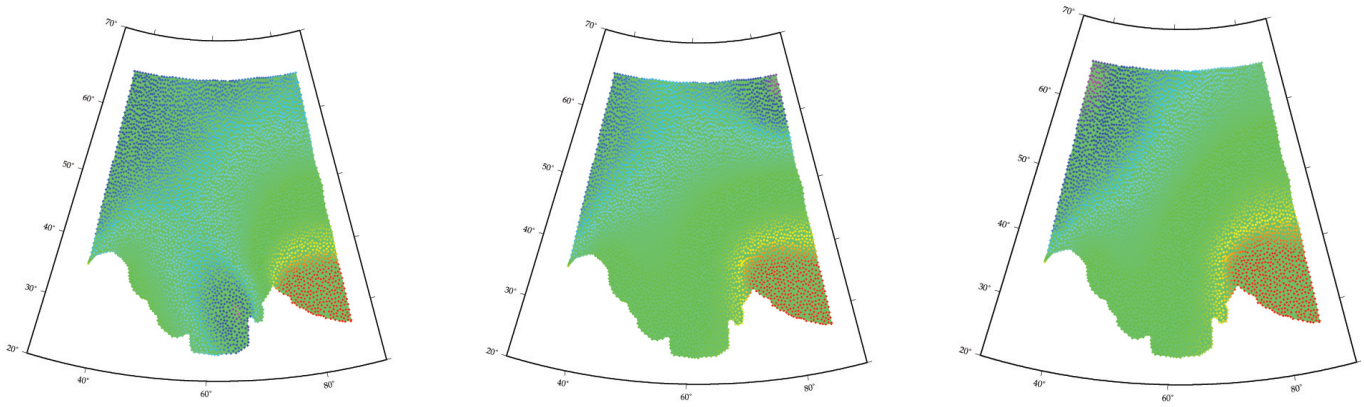

Figure 17: Magnitude of displacement for varying location of the anchor points. Red colours indicate high displacement magnitudes, blue to magenta colours indicate low to zero displacement magnitudes. In the left and central figure the anchor points were located at the bottom and top right of the modelled domain, showing low displacements around the anchor points where no low displacements are observed in the other figures. In the right figure the anchor points are placed top left, where the influence of the anchor points appears the lowest.

B On statistics

B.1 Approach

In this appendix methods used for calculating the averages and errors of our models and the comparison between these two models will be explained. This section will loosely follow the approach as explained in Mardia (1972), chapter 2 and as used by WR. To quantify the misfit between the modelled stresses and the observed stresses, the direction values found within certain domains need to be averaged ($\bar{\zeta}$ and $\bar{\beta}$) and the associated standard deviations ($\Delta\bar{\zeta}$ and $\Delta\bar{\beta}$) found. The size of the domain should account for both the resolution that can be resolved by the model and the spread and accuracy of the observations. A higher model resolution allows for smaller domains, but low accuracy of the observations requires a bigger domain. As such, the standard deviation consists of an observational error ($\Delta\bar{\beta}_{obs}$) and an error as a consequence of the spread within a domain ($\Delta\bar{\beta}_{spread}$ or $\Delta\bar{\zeta}_{spread}$).

The calculation of an average angle cannot simply be defined as

$$\bar{\beta}_m = \frac{\sum_{i=1}^{N} \beta_i}{N} \tag{17}$$

since there are always two solutions possible when averaging angles (with the exception where the angles are polar opposites). This problem can be solved by defining the angles over a complete circle, calculating the Cartesian coordinates, averaging these and converting back to the angles. This will return the average with the smallest misfit value. Since the angles in the model are defined over a range from 0 to 180 degrees rather than 0 to 360, initially every angle has to be multiplied by two. When averaging the model data, no information on the observational error is available and so the error margin will be only a consequence of the averaging process. Assume ζ_i as the i-th stress direction model result within a domain with a total of N model results.

$$\begin{aligned}
&\bar{c} = \left(\sum_i cos(2\zeta_i)\right)/N \qquad \bar{s} = \left(\sum_i sin(2\zeta_i)\right)/N \qquad R = \sqrt{\bar{c}^2 + \bar{s}^2} \\
&\Delta\bar{\zeta}_{spread} = \frac{1}{2}\sqrt{-2lnR} \\
&\bar{\zeta} = \frac{1}{2}\arctan\left(\frac{\bar{s}}{\bar{c}}\right) \qquad \Delta\bar{\zeta} = \Delta\bar{\zeta}_{spread}
\end{aligned} \tag{18}$$

When averaging the WSM data information on an observational error is available ($\pm 25°$) for all observations. When averaging these data the same approach as for the model data is used, but this time an observational error is taken into account. Take β_i as the i-th stress direction observation within a domain with an observation uncertainty $\Delta\beta_i$

$$\begin{aligned}
&w_i = 1/(\Delta\beta_i) \qquad W = \sum_i w_i \\
&\bar{c} = \left(\sum_i w_i cos(2\beta_i)\right)/W \qquad \bar{s} = \left(\sum_i w_i sin(2\beta_i)\right)/W \qquad R = \sqrt{\bar{c}^2 + \bar{s}^2} \\
&\Delta\bar{\beta}_{spread} = \frac{1}{2}\sqrt{-2lnR} \qquad \Delta\bar{\beta}_{obs} = 1/W \\
&\bar{\beta} = \frac{1}{2}\arctan\left(\frac{\bar{s}}{\bar{c}}\right) \qquad \Delta\bar{\beta} = \sqrt{\Delta\bar{\beta}^2_{spread} + \Delta\bar{\beta}^2_{obs}}
\end{aligned} \tag{19}$$

In every domain the modelled stress azimuth $\bar{\zeta}$ is then compared with the observed stress azimuth $\bar{\beta}$. The average misfit over the entire modelled domain ($\Delta\bar{\alpha}$), consisting of N domains is then

$$\Delta\bar{\alpha} = \frac{1}{N}\sum_{j}^{N} \left\|\bar{\zeta}_j - \bar{\beta}_j\right\| \tag{20}$$

with an uncertainty of

$$\widehat{\Delta\alpha} = \frac{1}{N}\sum_{j}^{N} \sqrt{\Delta\bar{\beta}_j^2 + \Delta\bar{\zeta}_j^2} \tag{21}$$

The plate wide average observation data error is

$$\widehat{\Delta\beta} = \frac{1}{N}\sum_{j}^{N} \Delta\bar{\beta}_j \tag{22}$$

and the plate wide average model error is

$$\widehat{\Delta\zeta} = \frac{1}{N}\sum_{j}^{N} \Delta\bar{\zeta}_j \tag{23}$$

The same equations are used for the calculation of the average directions and misfits in the Pamir subregion.

B.2 Results

Since averages of directions are compared the results will be directly influenced by the size and location of the averaging grid. For model verification purposes a data set where the uncertainty is the lowest is the best choice. However, to be able to compare results without further bias, the grid has to be the same for all models, despite the fact that in some case another grid might give a lower uncertainty. Since all results will be compared to the locked model, a grid is chosen that gives the lowest error margin on this specific model and that averaging grid is then applied to all models.

The observations are highly unevenly distributed and have a measurement error as well as that the averaging process will give a domain error. Especially for the observations the element size is important, for a trade-off occurs when varying the grid element size: increasing the domain size will decrease the measurement error but increase the domain error.

Several tests with different grid sizes and the element centres at 2 locations have been run for the locked model to find the location and grid element size with the lowest total uncertainty ($\widehat{\Delta\alpha}$). The results of these tests can be found in figure 18. This figure shows that the uncertainty varies with the exact location of the grid, but there does not appear to be a trend and so there is no optimal grid location. A definite optimum can be found in the uncertainty as a function of element size: the trade-off is clearly visible since the error margin increases when reaching too small or big domains, with the smallest uncertainty found at an element diameter of 0.5°. The average misfit between the model and the observation ($\Delta\bar{\alpha}$) as function of grid element size can also be found in this figure. The same result for grid location (no apparent optimum) is observed but a quite different trend for element size: the misfit decreases with increasing grid size. The preference is to have an accurate result rather than a good result however, so in this case the optimal element size is 0.5°, which is used in all our models.

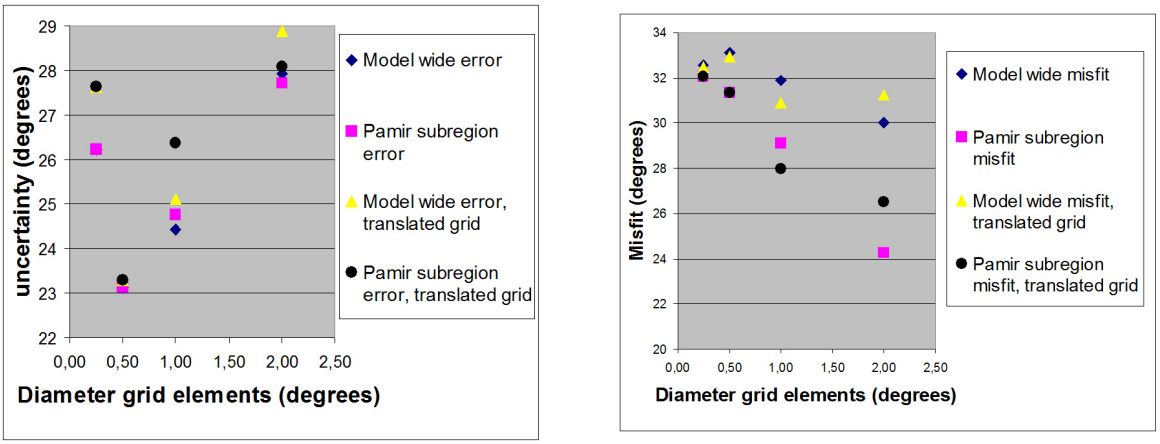

Figure 18: Left: the average data error $\widehat{\Delta\alpha}$ as a function of grid element size. Right: the average data misfit $\Delta\bar{\alpha}$ as a function of the grid element size.